

GALAXY CLUSTER PRESSURE PROFILES AS DETERMINED BY SUNYAEV ZEL'DOVICH EFFECT OBSERVATIONS WITH MUSTANG AND BOLOCAM II: JOINT ANALYSIS OF FOURTEEN CLUSTERS

CHARLES E. ROMERO^{1,2}, BRIAN S. MASON³, JACK SAYERS⁴ TONY MROCKOWSKI^{5,6}, CRAIG SARAZIN⁷, MEGAN DONAHUE⁸, ALESSANDRO BALDI⁸ TRACY E. CLARKE⁶, ALEXANDER H. YOUNG⁹, JONATHAN SIEVERS¹⁰, SIMON R. DICKER¹¹, ERIK D. REESE¹², NICOLE CZAKON^{4,13}, MARK DEVLIN¹¹, PHILLIP M. KORNGUT⁴, SUNIL GOLWALA⁴

(Dated: March 17, 2019)

ABSTRACT

We present pressure profiles of galaxy clusters determined from high resolution Sunyaev-Zel'dovich (SZ) effect observations of fourteen clusters, which span the redshift range $0.25 < z < 0.89$. The procedure simultaneously fits spherical cluster models to MUSTANG and Bolocam data. In this analysis, we adopt the generalized NFW parameterization of pressure profiles to produce our models. Our constraints on ensemble-average pressure profile parameters, in this study γ , C_{500} , and P_0 , are consistent with those in previous studies, but for individual clusters we find discrepancies with the X-ray derived pressure profiles from the ACCEPT2 database. We investigate potential sources of these discrepancies, especially cluster geometry, electron temperature of the intracluster medium, and substructure. We find that the ensemble mean profile for all clusters in our sample is described by the parameters: $[\gamma, C_{500}, P_0] = [0.3^{+0.1}_{-0.1}, 1.3^{+0.1}_{-0.1}, 8.6^{+2.4}_{-2.4}]$, for cool core clusters: $[\gamma, C_{500}, P_0] = [0.6^{+0.1}_{-0.1}, 0.9^{+0.1}_{-0.1}, 3.6^{+1.5}_{-1.5}]$, and for disturbed clusters: $[\gamma, C_{500}, P_0] = [0.0^{+0.1}_{-0.1}, 1.5^{+0.1}_{-0.2}, 13.8^{+1.6}_{-1.6}]$. Four of the fourteen clusters have clear substructure in our SZ observations, while an additional two clusters exhibit potential substructure.

Keywords: galaxy clusters: general — galaxy clusters

1. INTRODUCTION

Galaxy clusters are the largest gravitationally bound objects in the universe and thus serve as excellent cosmological probes and astrophysical laboratories. Within a galaxy cluster, the gas in the intracluster medium (ICM) constitutes 90% of the baryonic mass (Vikhlinin et al. 2006) and is directly observable in the X-ray due to bremsstrahlung emission. At millimeter and submillimeter wavelengths, the ICM is observable via the Sunyaev-Zel'dovich (SZ) effect (Sunyaev & Zel'dovich 1972): the inverse Compton scattering of cosmic microwave background (CMB) photons off of the hot ICM electrons. The thermal SZ is observed as an intensity decrement relative to the CMB at wavelengths longer

¹ Institut de Radioastronomie Millimétrique 300 rue de la Piscine, Domaine Universitaire 38406 Saint Martin d'Hères, France

² Author contact: romero@iram.fr

³ National Radio Astronomy Observatory, 520 Edgemont Rd., Charlottesville, VA 22903, USA

⁴ Department of Physics, Math, and Astronomy, California Institute of Technology, Pasadena, CA 91125, USA

⁵ ESO - European Organization for Astronomical Research in the Southern hemisphere, Karl-Schwarzschild-Str. 2, D-85748 Garching b. München, Germany

⁶ U.S. Naval Research Laboratory, 4555 Overlook Ave SW, Washington, DC 20375, USA

⁷ Department of Astronomy, University of Virginia, P.O. Box 400325, Charlottesville, VA 22904, USA

⁸ Physics and Astronomy Department, Michigan State University, 567 Wilson Rd., East Lansing, MI 48824, USA

⁹ MIT Lincoln Laboratories

¹⁰ Astrophysics & Cosmology Research Unit, University of KwaZulu-Natal, Private Bag X54001, Durban 4000, South Africa

¹¹ Department of Physics and Astronomy, University of Pennsylvania, 209 South 33rd Street, Philadelphia, PA, 19104, USA

¹² Department of Physics, Astronomy, and Engineering, Moorpark College, 7075 Campus Rd., Moorpark, CA 93021, USA

¹³ Academia Sinica, 128 Academia Road, Nankang, Taipei 115, Taiwan

than ~ 1.4 mm (frequencies less than ~ 220 GHz). The amplitude of the thermal SZ is proportional to the integrated line-of-sight electron pressure, and is often parameterized as Compton y : $y = (\sigma_T/m_e c^2) \int P_e dl$, where σ_T is the Thomson cross section, m_e is the electron mass, c is the speed of light, and P_e is the electron pressure.

Cosmological constraints derived from galaxy cluster samples are generally limited by the accuracy of mass calibration of galaxy clusters (e.g. Hasselfield et al. 2013; Reichardt et al. 2013), which is often calculated via a scaling relation with respect to some integrated observable quantity. Scatter in the scaling relations will then depend on the regularity of clusters and the adopted integration radius of the clusters. Determining pressure profiles of galaxy clusters provides an assessment of the relative impact and frequency of various astrophysical processes in the ICM and can refine the choice of integration radius of galaxy clusters to reduce the scatter in scaling relations.

In the core of a galaxy cluster, some observed astrophysical processes include shocks and cold fronts (e.g. Markevitch & Vikhlinin 2007), sloshing (e.g. Fabian et al. 2006), and X-ray cavities (McNamara & Nulsen 2007). It is also theorized that helium sedimentation should occur, most noticeably in low redshift, dynamically-relaxed clusters (Abramopoulos et al. 1981; Gilfanov & Sunyaev 1984) and recently the expected helium enhancement via sedimentation has been numerically simulated (Peng & Nagai 2009). This would result in an offset between X-ray and SZ derived pressure profiles if not accounted for correctly.

At large radii ($R \gtrsim R_{500}$),¹⁴ equilibration timescales

¹⁴ R_{500} is the radius at which the enclosed average mass density is 500 times the critical density, $\rho_c(z)$, of the universe

are longer, accretion is ongoing, and hydrostatic equilibrium (HSE) can be a poor approximation. Several numerical simulations show that the fractional contribution from non-thermal pressure increases with radius (Shaw et al. 2010; Battaglia et al. 2012; Nelson et al. 2014). For all three studies, non thermal pressure fractions between 15% and 30% are found at ($R \sim R_{500}$) for redshifts $0 < z < 1$. Additionally, clumping is expected to increase with radius (Kravtsov & Borgani 2012), and is expected to increase the scatter of pressure profiles at large radii (Nagai & Lau 2011) as well as biasing X-ray derived gas density high, and thus X-ray derived thermal pressure low (Battaglia et al. 2015).

By contrast, the intermediate region, between the core and outer regions of the galaxy cluster, is often the best region to apply self-similar scaling relations derived from HSE (e.g. Kravtsov & Borgani 2012). Moreover, both simulations and observations find low cluster-to-cluster scatter in pressure profiles within this intermediate radial range (e.g. Borgani et al. 2004; Nagai et al. 2007; Arnaud et al. 2010; Bonamente et al. 2012; Planck Collaboration et al. 2013; Sayers et al. 2013).

In recent years, the SZ community has often adopted the pressure profile presented in Arnaud et al. (2010) (hereafter, A10), who derive their pressure profiles from X-ray data from the REXCESS sample of 31 nearby ($z < 0.2$) clusters out to R_{500} and numerical simulations for larger radii. The adoption of the A10 pressure profile allows for the extraction of an integrated observable quantity which, via scaling relations, can then be used to determine the mass of the clusters. In this paper, we use high resolution SZ data to test the validity of this pressure profile in our sample of 14 clusters at intermediate redshifts.

There are many existing facilities capable of making SZ observations, but most have angular resolutions of one arcminute or larger. The MUSTANG camera (Dicker et al. 2008) on the 100 meter Robert C. Byrd Green Bank Telescope (GBT, Jewell & Prestage 2004) with its angular resolution of 9'' (full-width, half-maximum FWHM) is one of only a few SZ effect instruments with sub-arcminute resolution. However, MUSTANG's instantaneous field of view (FOV) of 42'' means that it is not sensitive to scales over $\sim 1'$. To probe a wider range of scales we complement our MUSTANG data with SZ data from Bolocam (Glenn et al. 1998). Bolocam is a 144-element bolometer array on the Caltech Submillimeter Observatory (CSO) with a beam FWHM of 58'' at 140 GHz and circular FOV with 8' diameter, which is well matched to the angular size of R_{500} ($\sim 4'$) of the clusters in our sample.

This paper is organized as follows. In Section 2 we describe the MUSTANG and Bolocam observations and reduction. In Section 3 we review the method used to jointly fit pressure profiles to MUSTANG and Bolocam data. We present results from the joint fits in Section 4 and compare our results to X-ray derived pressures in Section 6. Throughout this paper we assume a Λ CDM cosmology with $\Omega_m = 0.3$, $\Omega_\lambda = 0.7$, and $H_0 = 70$ km s $^{-1}$ Mpc $^{-1}$. For the remainder of the paper we denote the electron pressure as P , electron density as n_e , and electron temperature as T . The errors we report are 1σ (68.5% confidence) unless otherwise noted.

2. OBSERVATIONS AND DATA REDUCTION

2.1. Sample

Our cluster sample is based primarily on the Cluster Lensing And Supernova survey with Hubble (CLASH) sample (Postman et al. 2012). The CLASH sample has 25 massive galaxy clusters, 20 of which are selected from X-ray data (from *Chandra X-ray Observatory*, hereafter *Chandra*), and 5 based on exceptional lensing strength. These clusters have the following properties: $0.187 < z < 0.890$, $5.5 < k_B T$ (keV) < 15.5 , and $6.7 \times 10^{44} < L_{bol}$ (erg s $^{-1}$) < 90.8 . Thus, these clusters are large enough that we should expect to detect them with MUSTANG with a reasonable amount of time on the sky (on average, < 25 hours per cluster).

Of the 25 clusters in the CLASH sample, four are too far south to be observed with MUSTANG from Green Bank, WV. Of the remaining 21, we were able to observe fourteen given the available good weather and their limited visibility during the observational campaign from 2009 to 2014. Abell 209 was observed, but was relatively noisy and showed no trace of any detection. Our final sample includes thirteen CLASH clusters. We also include Abell 1835, a cluster of similar mass and redshift as the CLASH clusters, which was observed under the program GBT/09A-052. These clusters (Table 1) were also observed with Bolocam, and have been analyzed in Sayers et al. (2012, 2013); Czakon et al. (2015). The centroid differences between the *Archive of Chandra Cluster Entropy Profile Tables* (ACCEPT Cavagnolo et al. 2009) and Bolocam ($\Delta r_{X,SZ}$) are also listed as in Table 1. The total integration times of MUSTANG and Bolocam observations, along with detection significances, of our sample are listed in Table 2.

2.2. MUSTANG Observations and Reduction

MUSTANG is a 64 pixel array of Transition Edge Sensor (TES) bolometers arranged in an 8×8 array located at the Gregorian focus on the 100 m GBT. Operating at 90 GHz (81–99 GHz), MUSTANG has an angular resolution of 9'' and pixel spacing of $0.63f\lambda$ resulting in a FOV of 42''. More detailed information about the instrument can be found in Dicker et al. (2008).

Our observations and data reduction are described in detail in Romero et al. (2015), and we briefly review them here. Absolute flux calibrations are based on the planets Mars, Uranus, and Saturn; or the star Betelgeuse (α_{Ori}). At least one of these flux calibrators was observed at least once per night, and we find our calibration is accurate to a 10% RMS uncertainty. We also observe bright point sources every half hour to track our pointing and beam shape. To observe the target galaxy clusters, we employ Lissajous daisy scans with a 3' radius and in many of the clusters we broadened our coverage with a hexagonal pattern of daisy centers (with 1' offsets). For most clusters, the coverage (weight) drops to 50% of its peak value at a radius of 1.3'.

Processing of MUSTANG data is performed using a custom IDL pipeline. Raw data is recorded as time ordered data (TOD) from each of the 64 detectors. An outline of the data processing for each scan on a galaxy cluster is as follows:

(1) We define a pixel mask from the nearest preceding CAL scan; unresponsive detectors are masked out. The

Table 1
Cluster properties

Cluster	z	M_{500} ($10^{14} M_{\odot}$)	P_{500} (keV/cm 3)	R_{500} (kpc)	T_x^a (keV)	T_x^b (keV)	T_{mg} (keV)	Dynamical state	$\Delta r_{X,SZ}$ ($''$)
Abell 1835	0.253	12	0.00594	1490	9.0	10.0	7.49	CC	6.8
Abell 611	0.288	7.4	0.00445	1240	6.8	—	6.71	—	18.7
MACS1115	0.355	8.6	0.00545	1280	9.2	9.14	7.04	CC	34.8
MACS0429	0.399	5.8	0.00448	1100	8.3	8.55	5.56	CC	18.7
MACS1206	0.439	19	0.01059	1610	10.7	11.4	10.0	—	6.9
MACS0329	0.450	7.9	0.00596	1190	6.3	5.85	5.64	CC & D	14.8
RXJ1347	0.451	22	0.01171	1670	10.8	13.6	9.86	CC	9.6
MACS1311	0.494	3.9	0.00399	930	6.0	6.36	5.18	CC	27.7
MACS1423	0.543	6.6	0.00612	1090	6.9	6.81	5.50	CC	19.8
MACS1149	0.544	19	0.01228	1530	8.5	8.76	7.70	D	6.0
MACS0717	0.546	25	0.01490	1690	11.8	10.6	9.06	D	32.4
MACS0647	0.591	11	0.00923	1260	11.5	12.6	8.06	—	6.9
MACS0744	0.698	13	0.01199	1260	8.1	8.90	6.85	D	4.9
CLJ1226	0.888	7.8	0.01184	1000	12.0	11.7	11.3	—	15.3

Note. — z , M_{500} , and T_x^a are taken from Mantz et al. (2010); T_x^a is calculated from a single spectrum over $0.15R_{500} < r < R_{500}$ for each cluster. T_x^b is from Morandi et al. (2015), and is calculated over $0.15R_{500} < r < 0.75R_{500}$. T_{mg} is a fitted gas mass weighted temperature, (Section 6.2) determined by fitting the ACCEPT2 (Baldi 2014) temperature profiles to the gas mass weighted profile found in Vikhlinin (2006). The dynamical states: cool core (CC) and disturbed (D) are taken from (and defined in) Sayers et al. (2013). $\Delta r_{X,SZ}$ denotes the offset between the ACCEPT and Bolocam centroids.

Table 2
Bolocam and MUSTANG observational properties.

Cluster	z	R.A. (J2000)	Decl. (J2000)	$t_{obs,B}$ (hours)	Noise_B μK_{CMB} -amin	$A10_B$ (σ)	$t_{obs,M}$ (hours)	Noise_M $\mu\text{Jy/bm}$	$A10_M$ (σ)
Abell 1835	0.253	14:01:01.9	+02:52:40	14.0	16.2	28.9	8.6	53.4	10.0
Abell 611	0.288	08:00:56.8	+36:03:26	18.7	25.0	13.9	12.0	46.2	1.73
MACS1115	0.355	11:15:51.9	+01:29:55	15.7	22.8	16.3	10.0	56.4	8.66
MACS0429	0.399	04:29:36.0	-02:53:06	17.0	24.1	13.2	11.6	47.2	-0.02
MACS1206	0.439	12:06:12.3	-08:48:06	11.3	24.9	28.7	13.3	42.5	8.89
MACS0329	0.450	03:29:41.5	-02:11:46	10.3	22.5	17.4	13.1	39.9	8.63
RXJ1347	0.451	13:47:30.8	-11:45:09	15.5	19.7	45.3	1.9	276.	8.90
MACS1311	0.494	13:11:01.7	-03:10:40	14.2	22.5	11.3	10.6	64.5	0.71
MACS1423	0.543	14:23:47.9	+24:04:43	21.7	22.3	11.8	11.2	35.7	6.15
MACS1149	0.544	11:49:35.4	+22:24:04	17.7	24.0	22.0	13.9	32.7	-1.47
MACS0717	0.546	07:17:32.1	+37:45:21	12.5	29.4	31.3	14.6	27.1	3.05
MACS0647	0.591	06:47:49.7	+70:14:56	11.7	22.0	24.1	16.4	20.3	11.3
MACS0744	0.698	07:44:52.3	+39:27:27	16.3	20.6	17.8	7.6	48.5	7.67
CLJ1226	0.888	12:26:57.9	+33:32:49	11.8	22.9	13.7	4.9	85.6	9.43

Note. — Subscripts B and M denote Bolocam and MUSTANG properties respectively. Noise_B and $t_{obs,B}$ are those reported in Sayers et al. (2013). Noise_M is calculated on MUSTANG maps with $10''$ smoothing, in the central arcminute. t_{obs} are the integration times (on source) for the given instruments. $A10_B$ and $A10_M$ values indicate the significance (in σ) of P_0 when we fit a spherical $A10$ (Arnaud et al. 2010) profile (see Section 3.2.1).

CAL scan provides us with unique gains to be applied to each of the responsive detectors.

(2) A common mode template, polynomial, and sinusoid are fit to the data and then subtracted. The common mode is calculated as the arithmetic mean of the TOD across detectors.

(3) After the common mode and polynomial subtraction each scan is subjected to spike (glitch), skewness, and Allan variance tests and are flagged according to the following criteria. Glitches are flagged as 4σ excursions based on the median absolute deviation; The skewness threshold for flagging is 0.4. Flags based on Allan variance require the variance over a two second interval to be greater than 9 times the variance between each integration. Typical scan integration times were 150 seconds.

(4) Individual detector weights are calculated as $1/\sigma_i^2$,

where σ_i is the RMS of the non-flagged TOD for that detector.

(5) Maps are produced by gridding the TOD in $1''$ pixels in Right Ascension (R.A.) and Declination (Dec). A weight map is produced in addition to the signal map.

2.3. Bolocam Observations and Reduction

Bolocam is a 144-element camera that was a facility instrument on the Caltech Submillimeter Observatory (CSO) from 2003 until 2012. Its field of view is $8'$ in diameter, and at 140 GHz it has a resolution of $58''$ FWHM (Glenn et al. (1998); Haig et al. (2004)). The clusters were observed with a Lissajous pattern that results in a tapered coverage dropping to 50% of the peak value at a radius of roughly $5'$, and to 0 at a radius of $10'$. The Bolocam maps used in this analysis are $14' \times 14'$. The Bolocam

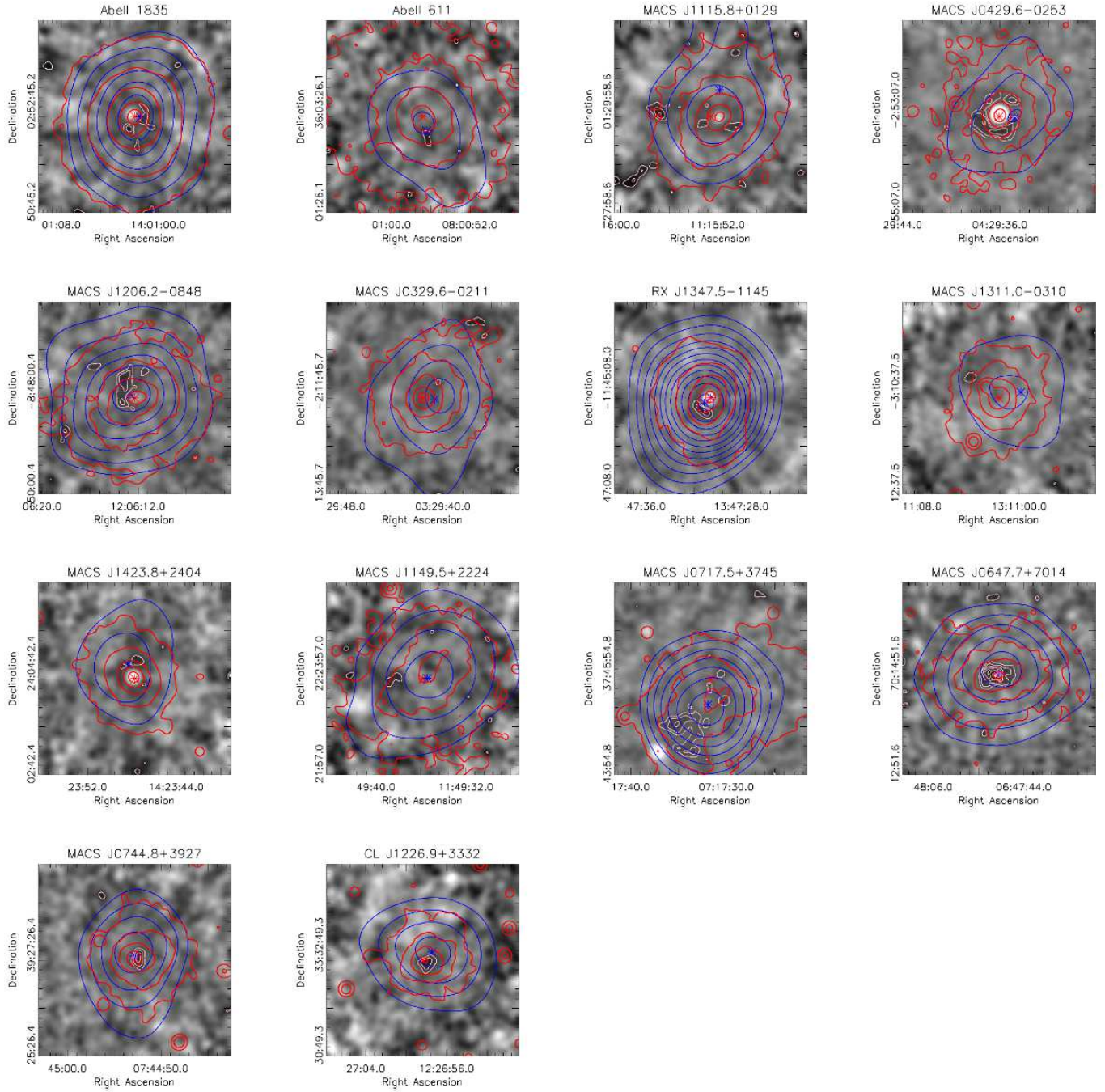


Figure 1. MUSTANG maps of the clusters in our sample. Pale contours are MUSTANG contours; blue contours are Bolocam. Both start at 3σ decrement, with 1σ intervals for MUSTANG and 2σ intervals for Bolocam. Red contours are X-ray surface brightness contours at arbitrary levels. The red asterisk is the ACCEPT centroid; the blue asterisk is the Bolocam centroid.

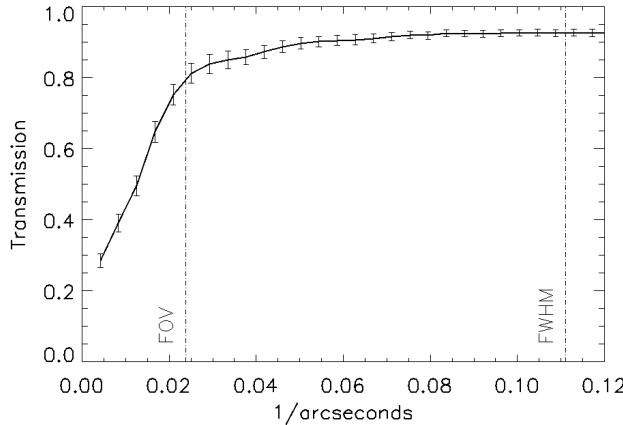


Figure 2. Effective average transfer function of our MUSTANG data reduction over our sample. The variations between cluster are less than 3%. For each cluster, attenuation is calculated based on simulated observations of 25 fake skies. The plotted one-dimensional transfer function is the weighted average of the transfer functions of individual clusters. The error bars show the scatter among cluster transfer functions. The transfer functions (transmission) of individual clusters are calculated as the square root of the ratio of the one dimensional power spectra of the observed fake sky and input fake sky. We have labelled the relevant angular wavenumbers for the FOV and FWHM.

cam data¹⁵ are the same as those used in Czakon et al. (2015) and Sayers et al. (2013); the details of the reduction are given therein, along with Sayers et al. (2011). The reduction and calibration is similar to that used for MUSTANG, and Bolocam achieves a 5% calibration accuracy and 5'' pointing accuracy.

3. JOINT MAP FITTING TECHNIQUE

3.1. Overview

The joint map fitting technique used in this paper is described in detail in Romero et al. (2015). We review it briefly here. The general approach follows that of a least squares fitting procedure, which assumes that we can make a model map as a linear combination of model components.

This linear combination can be written as:

$$\vec{d}_{mod} = \mathbf{A} \vec{a}_{mod}, \quad (1)$$

where d_{mod} is the total model, each column in \mathbf{A} is a filtered model component (Section 3.2), and \vec{a}_{mod} is an array of amplitudes of the components. There are up to four types of components for which we fit: a bulk component, point source(s), residual component(s), and a mean level. From these, we produce a sky model for the bulk component and point source to be filtered. The residual component is calculated directly as a filtered component.

We wish to fit \vec{d}_{mod} to our data, \vec{d} , and allow for a calibration offset between Bolocam and MUSTANG data. To accomplish this, we define our data vector as:

$$\vec{d} = [\vec{d}_B, k\vec{d}_M, k], \quad (2)$$

¹⁵ Bolocam data is publicly available at http://irsa.ipac.caltech.edu/data/Planck/release_2/ancillary-data/bolocam/.

where \vec{d}_B is the Bolocam data, \vec{d}_M is the MUSTANG data, and k is the calibration offset of MUSTANG relative to Bolocam, to which we apply an 11.2% Gaussian prior derived from the MUSTANG and Bolocam calibration uncertainties.

We use the χ^2 statistic as our goodness of fit:

$$\chi^2 = (\vec{d} - \vec{d}_{mod})^T \mathbf{N}^{-1} (\vec{d} - \vec{d}_{mod}), \quad (3)$$

where \mathbf{N} is the covariance matrix; however, because we wish to fit for k in addition to the amplitude of model components, we no longer have completely linearly independent variables, and thus we employ MPFIT (Markwardt 2009) to solve for these variables. Confidence intervals are derived from χ^2 values over the parameter space searched (Section 3.3), and adjusted based on monte carlo simulations (Romero et al. 2015).

Our approach is to fix the shape and position of point sources and residuals (if any), fitting only their amplitudes. We explore the shape of the bulk ICM component parametrically, where each point in the parametric space may be forward modeled (Section 3.3). At each point in the parameter space we do a linear least squares fit followed by a nonlinear minimization over k , the Bolocam pointing, and \vec{a}_{mod} .

3.2. Components

In order to produce component maps, it is necessary to account for the response of both instruments and imaging pipeline filter functions. For Bolocam, we use the transfer function provided. For MUSTANG, we perform simulated observations, processing the sky models in the same manner that real data is processed.

3.2.1. Bulk ICM

As in Romero et al. (2015), the bulk component is taken to be a spherically symmetric 3D electron pressure profile as parameterized by a generalized Navarro, Frenk, and White profile (hereafter, gNFW Navarro et al. 1997; Nagai et al. 2007):

$$\tilde{P} = \frac{P_0}{(C_{500}X)^\gamma [1 + (C_{500}X)^\alpha]^{(\beta - \gamma)/\alpha}} \quad (4)$$

where $X = R/R_{500}$, and C_{500} is the concentration parameter; one can also write $(C_{500}X)$ as (R/R_s) , where $R_s = R_{500}/C_{500}$. \tilde{P} is the electron pressure in units of the characteristic pressure P_{500} . This pressure profile is integrated along the line of sight to produce a Compton y profile, given as

$$y(r) = \frac{P_{500}\sigma_T}{m_e c^2} \int_{-\infty}^{\infty} \tilde{P}(r, l) dl \quad (5)$$

where $R^2 = r^2 + l^2$, r is the projected radius, and l is the distance from the center of the cluster along the line of sight. Once integrated, $y(r)$ is gridded as $y(\theta)$ and is realized as two maps with the same astrometry as the MUSTANG and Bolocam data maps (pixels of 1'' and 20'' on a side, respectively). In each case, we convolve the Compton y map by the appropriate beam shape. For Bolocam we use a Gaussian with FWHM = 58'', and for MUSTANG we use the double Gaussian, representing the GBT main beam and stable error beam (Romero et al. 2015).

Table 3
Point source flux densities

Cluster	R.A. (J2000)	Dec (J2000)	S_{90} (mJy)	S_{140} (mJy)
Abell 1835	14:01:02.07	+2:52:47.52	1.37 ± 0.08	0.7 ± 0.2
MACS 1115	11:15:51.82	+1:29:56.82	1.04 ± 0.11	—
MACS 0429	04:29:35.97	-2:53:04.74	7.67 ± 0.84	6.0 ± 1.8
MACS 1206	12:06:12.11	-8:48:00.85	0.75 ± 0.08	—
RXJ1347	13:47:30.61	-11:45:09.48	7.40 ± 0.58	4.0 ± 1.2
MACS 1423	14:23:47.71	+24:04:43.66	1.36 ± 0.13	0.7 ± 0.2
MACS 0717	07:17:37.03	+37:44:24.00	2.08 ± 0.25	—
CLJ1226	12:27:00.01	+33:32:42.00	0.36 ± 0.11	—

Note. — S_{90} is the best fit flux density to MUSTANG, and S_{140} is the assumed flux density in the Bolocam maps (at 140 GHz). The location of the point source is reported from the fitted centroid to the MUSTANG data. The conversion from mJy to the equivalent μK_{CMB} is given as: $S_{140}(\text{mJy/bm}) \sim S_{140}/20(\mu\text{K}_{CMB})$.

3.2.2. Point Sources

Point sources are treated in the same manner as in Romero *et al.* (2015). All compact sources in our sample are well modelled as a point source. We clearly detect point sources in Abell 1835, MACS 1115, MACS 0429, MACS 1206, RXJ1347, MACS 1423, and MACS 0717 in the MUSTANG maps. While no point source is evident from our raw MUSTANG map, a point source is identified by NIKA (Adam *et al.* 2015) in CLJ1226, which is posited to be a submillimeter galaxy (SMG) behind the cluster. That point source is distinct from the point source seen in Korngut *et al.* (2011), which is not evident in our map. The point source in MACS 0717 is due to a foreground elliptical galaxy (Mroczkowski *et al.* 2012). All of the remaining point sources (six) are coincident (within 3'' of reported coordinates) with the BCGs of their respective clusters (Crawford *et al.* 1999; Donahue *et al.* 2015). Moreover, of these six BCGs, four of them exhibit “unambiguous UV excess” (Donahue *et al.* 2015). The remaining two are Abell 1835 and MACS 1206. The UV excess in MACS 1206 may be due to lensed background systems (Donahue *et al.* 2015). Abell 1835 is not in the CLASH sample and thus was not included in Donahue *et al.* (2015). However, it was observed by O’Dea *et al.* (2010) and found to have a far UV flux corresponding to a star formation rate of $11.7 M_{\odot}$ per year, which fits within the SFR range ($5 - 80 M_{\odot} \text{ yr}^{-1}$) of the UV excess BCGs found in (Donahue *et al.* 2015). For the Bolocam images, the point sources in Abell 1835, MACS 0429, RXJ1347, and MACS 1423 have been subtracted based on an extrapolation of a power law fit to the 1.4 GHz NVSS (Condon *et al.* 1998) and 30 GHz SZA (Mroczkowski *et al.* 2009) measurements (Sayers *et al.* 2012). The flux densities for the point sources fitted are shown in Table 3.

3.2.3. Residual Components

Residual components are selected primarily based on peak decrements exceeding 4σ within the central arcminute of smoothed MUSTANG residual maps, which are not well fitted by a bulk model. We fit residual components for MACS 1206, RXJ 1347, MACS 0717 and MACS 0744. The residual component for MACS 0717 is coincident with subcluster C as identified in Ma *et al.* (2009), and has a centroid outside the central arcminute, but the features in the MUSTANG map extend into the

central arcminute. Although we do not fit for residual components in Abell 611 and MACS 1115, we report properties of potential residual components for these two clusters. We do not fit the residual component for Abell 611 because the peak significance is not 4σ and the bulk cluster model appears to account for much of the decrement. For MACS 1115, the residual component is outside the central arcminute and does not affect our fit.

To model the shape of residual component, we fit a two dimensional Gaussian to the selected pixels (those below -3σ). This Gaussian is then fit to the unsmoothed MUSTANG data map (in units of Compton y) with only its amplitude is allowed to vary to obtain the results presented in Table 4.

3.2.4. Mean Level

Similar to Czakon *et al.* (2015), we wish to account for a mean level (signal offset) in the MUSTANG maps. We do not wish to fit for a mean level simultaneously as a bulk component given the degeneracies. Therefore, to determine the mean level independent of the other components, we create a MUSTANG noise map and calculate the mean within the inner arcminute for each cluster. This mean is then subtracted before the other components are fit.

3.3. Parameter Space

As in Romero *et al.* (2015), we fix MUSTANG’s centroid, but allow Bolocam’s pointing to vary by $\pm 10''$ in RA and Dec with a prior on Bolocam’s radial pointing accuracy with an RMS uncertainty of $5''$. Our approach to find the absolute calibration offset between Bolocam and MUSTANG is the same as in Romero *et al.* (2015) (see also Section 3.1).

In Romero *et al.* (2015), we performed a grid search over γ and C_{500} , marginalizing over P_0 , where α and β are fixed to values determined from A10. To determine the impact of our choice of fixed α and β , we explored how the profile shapes change when different, fixed, values of α and β are adopted. In all cases, we find the pressure profile shapes are in very good agreement with one another and that the differences in χ^2 values are statistically consistent. Thus, our fits are not sensitive to the exact choice of α and β .

We search over $0 < \gamma < 1.3$ in steps of $\delta\gamma = 0.1$, and over $0.1 < C_{500} < 3.3$ in steps of $\delta C_{500} = 0.1$. This choice of parameter space searched is determined by computation requirements (largely in filtering maps) and covering a sufficient range of values. To create models in finer steps than $\delta\gamma$ and δC_{500} , we interpolate filtered model maps from nearest neighbors from the grid of original filtered models.

3.3.1. Centroid Choice

The default centroids used when gridding our bulk ICM component are the ACCEPT centroids. Given the offsets between ACCEPT and Bolocam centroids (Table 1), we perform a second set of fits where we grid the bulk ICM component using the Bolocam centroids and we do not find significant changes in the fitted gNFW parameters (Section 4). The ACCEPT centroid are taken to be the X-ray peaks unless the centroiding algorithm produced a centroid more than 70 kpc from

Table 4
Parameters of Residual Components from MUSTANG

Cluster	RA (J2000)	Dec (J2000)	Modeled Peak y (10^{-5})	FWHM _A ($''$)	FWHM _B ($''$)	θ (deg.)	Fitted Peak y (10^{-5})
Abell 611	8:00:56.20	36:03:00.08	8.4	20.7	35.3	70	—
MACS 1115	11:15:56.66	1:30:02.82	14	17.8	28.8	48	—
MACS 1206	12:06:12.91	-8:47:33.48	7.6	23.5	23.5	155	3.6 ± 0.7
RXJ1347	13:47:31.06	-11:45:18.38	42	12.2	30.1	48	52 ± 9
MACS 0717	7:17:34.01	37:44:49.73	4.4	58.9	58.9	—	4.6 ± 1.1
MACS 0744	7:44:52.22	39:27:28.71	11	17.0	23.5	91	9.0 ± 2.8

Note. — Residual components modeled with a two dimensional Gaussian with associated. θ is measured CCW (going east) from due north.

the X-ray peak, in which case they adopt that centroid (Cavagnolo et al. 2008).

4. SZ PRESSURE PROFILE CONSTRAINTS

We have constrained the gNFW parameters P_0 , C_{500} , and γ for fourteen individual clusters and present these constraints in Table 5. Given that we find minimal differences between the fitted parameters using either the ACCEPT or Bolocam centroids, we report the results using the ACCEPT centroids. We find that six of our sample of fourteen have a best fit $\gamma = 0$, where we do not allow $\gamma < 0$. We find that our range of C_{500} is sufficient, and that it is generally found to be $0.5 < C_{500} < 2.0$.

We are further interested in comparing our pressure profile constraints, individually, and as a sample, to previous constraints. To compare to the pressure profiles from ACCEPT2 (Baldi 2014), we fit gNFW profiles to the deprojected pressure profiles of our cluster sample (Section 6.1). We adopt B14 to refer to the ensemble pressure profiles fit to ACCEPT2 data for our sample of 14 clusters. Individually, we find discrepancies in pressure profiles, but as an ensemble there is relatively good agreement. Moreover, the average pressure profile for the 14 clusters has parameter values which are very similar to those found using X-ray data in Arnaud et al. (2010). This can also be seen in Figure 4, where the A10 and B14 pressure profiles are generally consistent to the profile from this work (R16), where deviations are $< 30\%$ over $0.03R_{500} < r < R_{500}$ for A10 and $< 50\%$ for B14. While all 14 clusters in this work are in Sayers et al. (2013) (hereafter S13), we note that they find a consistently higher average pressure profile. Furthermore, the average pressure profile found by Planck Collaboration et al. (2013) (hereafter P13) is also higher than our average profiles at both large and small radii. In Figure 4 we also include a comparison to the pressure profile determined from simulations in Nagai et al. (2007), denoted as N07.

While our average pressure profiles are in excellent agreement with the previously derived pressure profiles in the region $0.1R_{500} < r < R_{500}$, we see deviations at small and large radii. It is not too surprising that our fits agree with A10 at large radii, as we have fixed α and β to the A10 values. Despite our fourteen clusters being included in the BOXSZ sample (Sayers et al. 2013), we see that S13 shows higher pressure at all radii. S13, fixing the slope of γ , present a higher pressure at small radii than found here, where the MUSTANG data provide stronger constraints on the pressure gradients in the cluster core and suggest they are often weaker than pre-

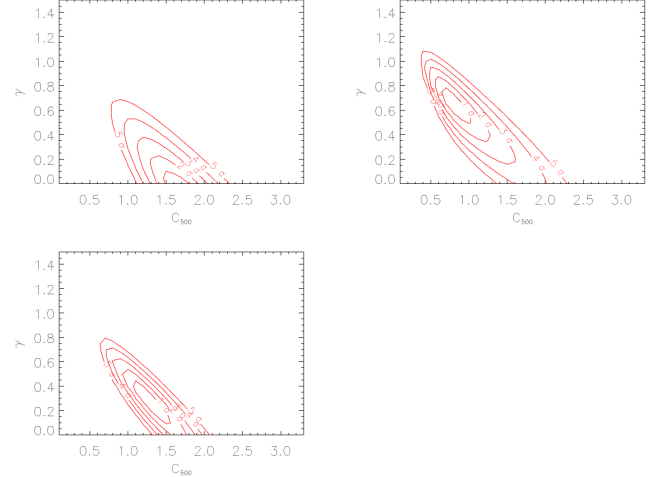


Figure 3. Confidence intervals over all disturbed clusters (upper left panel), cool-core clusters (upper right panel), and the entire sample (lower left panel). Cool core clusters include: Abell 1835, MACS 1115, MACS 0429, MACS 0329, RXJ 1347, MACS 1311 and MACS 1423. Disturbed clusters include: MACS 0329, MACS 1149, MACS 0717, and MACS 0744.

viously thought. At larger radii, our restriction of α and β again explain our reduced pressure relative to S13.

We further consider the ratio of cluster pressure profiles from our work (P_{SZ}) to the pressure profiles from other works. For comparisons with A10, P13, and S13, we take P_{A10} , P_{P13} , and P_{S13} to be the gNFW profile which each respective work had fit to their entire sample. For any of these sets (A10, P13, or S13), the ratio P_{SZ}/P_{set} is calculated for each cluster, where only P_{SZ} changes for each cluster. To compare P_{SZ} to ACCEPT2 (P_{XRAY}), we fit a gNFW profile to ACCEPT2 data (Section 6.1) for each cluster, and thus compare unique P_{SZ} and P_{XRAY} pressure profiles for each cluster. These ratios are shown in Figure 5, where the shaded regions are influenced both by statistical errors and scatter.

4.1. Fits with $\gamma = 0$

In 6 of our 14 clusters we find best fit pressure profiles with $\gamma = 0$, the limit we impose as a prior. There is no clear segregation based on dynamical state or presence of central point source. Here, we consider two effects which could spuriously bias the cluster central pressures: our choice of centroid and the mis-subtraction of a central point source.

As it stands, finding slopes in the cores of galaxy clusters that are fit with $\gamma = 0$ is not unprecedented; A10

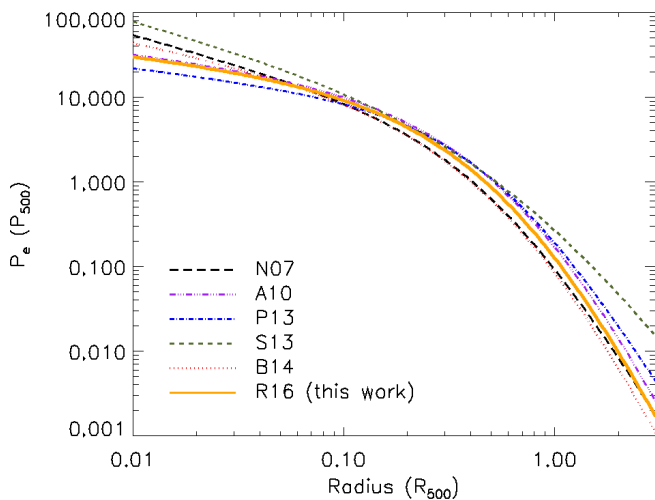


Figure 4. Pressure profiles from this (R16) and other works. We observe that for our fourteen clusters, the ACCEPT2 data (B14) falls below R16, whereas A10; P13, and S13 show higher pressure at large radii. The pressure profile N07 also agrees well with our work, but shows a steeper inner profile.

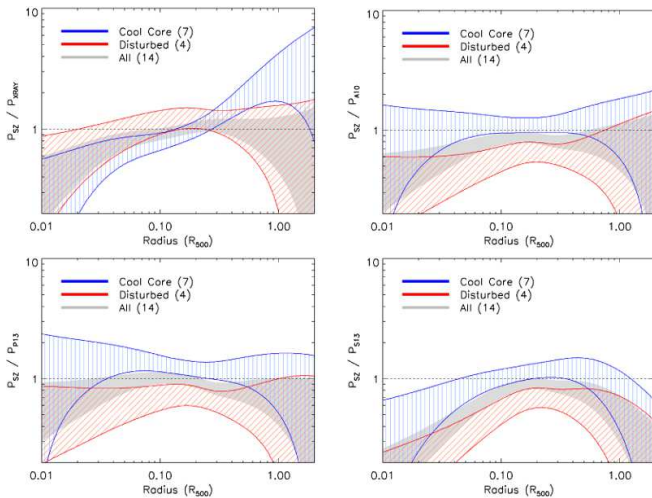


Figure 5. Pressure ratios as compared to different sets, plotted as the central 68% confidence intervals. The ensemble pressure ratios relative to ACCEPT2 ($P_{X\text{RAY}}$) are calculated per cluster and weighted by the error in the ratio (per radial bin). For the other pressure ratios, the ratio is again calculated per individual cluster, but the comparison pressure profile is the gNFW profile for the entire dataset, respectively (i.e. A10, P13, or S13). These ratios are weighted in the same manner.

find six of their 31 analyzed clusters in the REXCESS sample have $\gamma = 0$, where all gNFW parameters except β were fit for individual clusters. They find a similar range in C_{500} as we do. They fit for α , which is fit by the range $0.3 < \alpha < 2.5$ over their sample. While A10 is a local ($z < 0.2$) sample, Mantz *et al.* (2016) find $\gamma = -0.01$, using *Chandra* data, for their sample of 40 galaxy clusters of $0.07 < z < 1.10$. Moreover, in an analysis of X-ray (*Chandra*) data from observations of 80 clusters, McDonald *et al.* (2014) find $\gamma = 0$ for their low redshift ($0.3 < z < 0.6$), non-cool-core clusters, and similarly

shallow inner pressure profile slope ($\gamma = 0.05$) for the high redshift ($0.6 < z < 1.2$) non-cool-core clusters. Although these previous studies indicate that $\gamma = 0$ is relatively common, we explore whether systematics related to either our data or analysis methods may produce this results in our fits.

Shallow slopes in the cores of clusters could be suggestive of a centroid offset either between MUSTANG and Bolocam or between SZ and X-ray data. Given the MUSTANG and Bolocam pointing accuracies ($2''$ and $5''$, respectively), it is unlikely that the centroid offsets between MUSTANG and Bolocam are driving the fits to shallow slopes. The difference between SZ (Bolocam) centroids and ACCEPT centroids (Table 1) are large relative to pointing accuracies and thus potentially more important. However, when we adopt Bolocam’s centroid we find negligible change to the SZ pressure profile as compared to adopting the ACCEPT centroid.

Individually, the Bolocam and MUSTANG data sets yield consistent fits with each other, where changes in best fit parameters generally occur along the shallow gradient in confidence intervals (i.e. along the degeneracy between C_{500} , and γ).

Additionally, we consider the impact of the assumed flux densities of point sources in the Bolocam maps. There are four clusters (Abell 1835, MACS 0429, RXJ 1347, and MACS 1423) where it was necessary to extrapolate a 140 GHz flux density from lower frequency measurements in order to analyze the Bolocam data (Sayers *et al.* 2013). For points sources other than those in MACS 0429 and RXJ 1347, their uncertainty is less than the noise in the Bolocam maps. Moreover, in all but MACS 0429, the point source uncertainty is considerably less than the peak Bolocam decrement and miscalculations of the point source flux densities in these clusters will not significantly change our results. Therefore, we are left with only MACS 0429 where we believe that the treatment of the point source may affect our results non-trivially.

Only two (MACS 0429 and MACS 1423) of these four clusters are fit by notably low γ values. In addition, for the remaining four clusters in which MUSTANG detects a point source, the Bolocam maps assume no point source contamination. Of these remaining clusters, only MACS 0717 is fit by a notably low γ , and that is best attributed to the dynamics of the cluster (Section A.11).

We also consider that our treatment of point sources in the MUSTANG maps may leave residual emission from point sources, either due to our fitting procedure or the assumption that our assumed point source has a non-trivial extent. Our point source treatment was designed and extensively tested (e.g. Romero *et al.* 2015) to accurately remove point sources. In the case of Abell 1835, Romero *et al.* (2015) find good agreement between the MUSTANG and ALMA (McNamara *et al.* 2014) point source flux density.

5. INTEGRATED COMPTON Y SCALING RELATIONS

We calculate integrated Compton Y values at R_{500} due to the expected minimal scatter at intermediate radii (e.g. Kravtsov & Borgani 2012). We use R_{500} derived from X-ray observations (Mantz *et al.* 2010), and calcu-

Table 5
Summary of Fitted Pressure Profiles

Cluster	R_{500}^a (Mpc)	$Y_{cyl}(R_{500})$ (10^{-5} Mpc 2)	$Y_{sph}(R_{500})$ (10^{-5} Mpc 2)	$10^3 P_{500}^a$ keV cm $^{-3}$	P_0	C_{500}	α	β	γ	k	χ^2	d.o.f.
Abell 1835	1.49	$26.75^{+6.05}_{-6.15}$	$21.81^{+4.12}_{-4.49}$	5.94	2.15 ± 0.07	$0.77^{+0.23}_{-0.17}$	1.05	5.49	$0.78^{+0.12}_{-0.13}$	1.08	0.99	12880
Abell 611	1.24	$9.67^{+4.85}_{-2.57}$	$8.73^{+3.68}_{-2.21}$	4.45	35.43 ± 2.46	$2.00^{+0.40}_{-0.30}$	1.05	5.49	$0.00^{+0.15}_{-0.15}$	0.96	1.02	12882
MACS 1115	1.28	$30.28^{+7.32}_{-6.30}$	$20.10^{+3.84}_{-3.52}$	5.45	0.67 ± 0.04	$0.35^{+0.15}_{-0.10}$	1.05	5.49	$0.87^{+0.18}_{-0.27}$	1.11	1.04	12875
MACS 0429	1.10	$30.41^{+7.72}_{-6.88}$	$19.57^{+4.00}_{-3.74}$	4.48	11.01 ± 0.77	$0.59^{+0.11}_{-0.09}$	1.05	5.49	$0.00^{+0.15}_{-0.15}$	1.00	1.03	12875
MACS 1206	1.61	$61.52^{+12.49}_{-12.63}$	$48.16^{+8.19}_{-8.27}$	10.59	2.39 ± 0.10	$0.74^{+0.16}_{-0.14}$	1.05	5.49	$0.51^{+0.14}_{-0.16}$	1.09	1.01	12874
MACS 0329	1.19	$13.38^{+3.83}_{-2.99}$	$11.86^{+2.93}_{-2.37}$	5.93	9.30 ± 0.50	$1.18^{+0.72}_{-0.28}$	1.05	5.49	$0.41^{+0.19}_{-0.41}$	1.03	0.99	12876
RXJ1347	1.67	$42.47^{+8.29}_{-6.81}$	$37.80^{+5.78}_{-5.11}$	11.71	3.24 ± 0.08	$1.18^{+1.02}_{-0.48}$	1.05	5.49	$0.80^{+0.30}_{-0.70}$	1.15	0.99	12880
MACS 1311	0.93	$17.18^{+3.80}_{-3.49}$	$10.08^{+1.79}_{-1.73}$	3.99	2.75 ± 0.22	$0.35^{+0.15}_{-0.05}$	1.05	5.49	$0.41^{+0.34}_{-0.41}$	0.98	1.00	12881
MACS 1423	1.09	$10.35^{+4.00}_{-2.73}$	$8.89^{+2.53}_{-2.07}$	6.12	22.39 ± 1.71	$1.58^{+0.22}_{-0.48}$	1.05	5.49	$0.00^{+0.35}_{-0.35}$	1.04	0.98	12876
MACS 1149	1.53	$56.87^{+8.04}_{-9.00}$	$41.62^{+4.99}_{-5.67}$	12.28	5.50 ± 0.25	$0.83^{+0.07}_{-0.03}$	1.05	5.49	$0.00^{+0.05}_{-0.05}$	0.87	1.00	12876
MACS 0717	1.69	$54.16^{+9.56}_{-8.72}$	$48.06^{+7.71}_{-6.95}$	14.90	21.88 ± 0.68	$2.00^{+0.20}_{-0.20}$	1.05	5.49	$0.00^{+0.05}_{-0.05}$	0.49	1.03	13583
MACS 0647	1.26	$34.06^{+10.21}_{-7.76}$	$26.33^{+5.37}_{-5.37}$	9.23	2.78 ± 0.11	$0.70^{+0.30}_{-0.20}$	1.05	5.49	$0.60^{+0.15}_{-0.20}$	1.14	1.01	12876
MACS 0744	1.26	$15.10^{+4.50}_{-3.01}$	$13.20^{+3.18}_{-2.29}$	11.99	13.15 ± 0.81	$1.71^{+0.29}_{-0.21}$	1.05	5.49	$0.00^{+0.15}_{-0.15}$	0.90	1.02	12875
CLJ1226	1.00	$10.50^{+2.65}_{-1.94}$	$9.46^{+2.03}_{-1.60}$	11.84	19.29 ± 1.25	$1.90^{+0.60}_{-0.50}$	1.05	5.49	$0.29^{+0.36}_{-0.29}$	0.92	1.03	12875
All	—	—	—	—	8.58 ± 2.37	$1.3^{+0.1}_{-0.1}$	1.05	5.49	$0.3^{+0.1}_{-0.1}$	—	—	—
Cool Core	—	—	—	—	3.55 ± 1.53	$0.9^{+0.1}_{-0.1}$	1.05	5.49	$0.6^{+0.1}_{-0.1}$	—	—	—
Disturbed	—	—	—	—	13.81 ± 1.55	$1.6^{+0.1}_{-0.1}$	1.05	5.49	$0.0^{+0.1}_{-0.1}$	—	—	—
All (A10)	—	—	—	—	$8.403h_{70}^{-3/2}$	1.18	1.05	5.49	0.31	—	—	—
Cool core (A10)	—	—	—	—	$3.249h_{70}^{-3/2}$	1.13	1.22	5.49	0.78	—	—	—
Disturbed (A10)	—	—	—	—	$3.202h_{70}^{-3/2}$	1.08	1.41	5.49	0.38	—	—	—

Note. — Results from our pressure profile analysis. Y_{sph} is calculated using the tabulated value of R_{500} . ^aValues of R_{500} and P_{500} are taken from Sayers et al. (2013). We have assumed A10 values of α and β . The findings from A10 are reproduced in the last three rows. The h_{70} dependence is included for explicit replication of A10 results; all P_0 values have this dependence (the assumed cosmologies are the same).

late Y_{sph} , given by:

$$Y_{sph}(R) = \frac{\sigma_T}{m_e c^2} \int_0^R P(r') 4\pi r'^2 dr' \quad (6)$$

and Y_{cyl} , which is given by:

$$Y_{cyl}(R) = \frac{\sigma_T}{m_e c^2} \int_0^R 2\pi r dr \int_r^{R_b} \frac{2r' P(r') dr'}{\sqrt{r'^2 - r^2}}, \quad (7)$$

where we adopt $R_b = R_{500}$ as in A10. The error bars on $Y_{sph}(R_{500})$ and $Y_{cyl}(R_{500})$ are found by calculating the respective quantities from the pressure profile fits over the 1000 noise realizations, and taking the values encompassing the middle 68%. We take M_{500} from Mantz et al. (2010), who arrive at M_{500} in the following steps: (1) calculate R_{500} using a ratio of $R_{500}/R_{2500} \sim 2.3$ assuming a NFW profile with concentration parameter $c = 4$, (2) calculate $M_{gas,500}$, the total gas mass enclosed in R_{500} from deprojected gas mass (non-parametric) profiles, (3) determine the gas mass fraction, $f_{gas}(r_{500})$, by fitting a power law model to $f_{gas}(r)$ from simulations, and (4) calculate M_{500} as $(M_{gas}(r_{500}))((1+B)f_{gas}(r_{500}))^{-1}$, where $B = 0.03 \pm 0.06$ is a systematic fractional bias. Mantz et al. (2010) note that the dominant source of systematic uncertainty associated with M_{500} comes from the uncertainty in the assumed $f_{gas}(r_{2500}) = 0.1104$, which was used in calibrating $f_{gas}(r_{500}) \approx 0.115$.

We compare our $Y_{sph}(R_{500}) - M_{500}$ relation to that of A10 in Figure 6. The $Y_{sph} - M_{500}$ scaling relation

calculated in A10 is given as:

$$h(z)^{-2/3} Y_{sph}(xR_{500}) = A_x \left[\frac{M_{500}}{3 \times 10^{14} h_{70}^{-1} M_\odot} \right]^\alpha, \quad (8)$$

where $\alpha = 1.78$, $A_x = 2.925 \times 10^{-5} I(x) h_{70}^{-1} \text{Mpc}^2$, and $I(1) = 0.6145$. We find six of fourteen clusters that are more than 2σ in Y_{sph} from the scaling relation. When we consider the mass uncertainty, that number drops to three. While our sample size is small, the tendency of cool core clusters to lie above the scaling relation and of disturbed clusters to lie below the scaling relation is interesting. Regardless of cluster type, our sample does show a more shallow $Y_{sph,500} - M_{500}$ slope (1.06 ± 0.13) than the predicted self similar slope ($5/3$) or 1.78 found in A10. This is consistent with the slope found for the BOXSZ sample by Czakon et al. (2015) for $Y_{cyl,2500} - M_{2500}$ of 1.06 ± 0.12 .

6. COMBINING SZ AND X-RAY DATA

The observed SZ and X-ray signal from galaxy clusters differ in their dependence upon the physical properties in the intracluster medium (ICM). This difference has, in the past, been exploited to make calculations of the Hubble parameter, H_0 , assuming spherical geometry of galaxy clusters. However, one can also relax the spherical assumption and use the differences in SZ and X-ray observables to estimate effects such as helium sedimentation, or derive the ICM electron temperature without X-ray spectral information. These cannot all be independently constrained. Helium sedimentation will produce a higher P_X relative to P_{SZ} . However, within the pre-

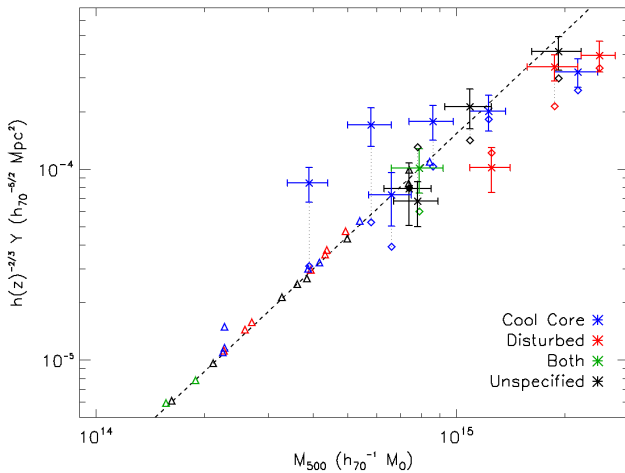


Figure 6. $Y_{sph,SZ}(R_{500})$ as calculated in this work (Table 5), and M_{500} as calculated from Mantz et al. (2010). The scaling relation (dashed line) and triangles are from Arnaud et al. (2010) and Pratt et al. (2010). The diamonds are $Y_{sph,X}(R_{500})$ as calculated from the gNFW fits to the ACCEPT2 pressure profiles. MACS 1311 and MACS 0429 are the notable outliers above the scaling relation.

dicted range of helium sedimentation (e.g. Peng & Nagai 2009), we lack sufficient sensitivity to constrain it. Thus, we investigate cluster geometry and electron temperature individually, and conclude that differences in the SZ and X-ray spherically derived pressure profiles cannot be explained exclusively by either cluster elongation or ICM temperature distribution.

We compare our SZ data (primarily the pressure profiles) to the ACCEPT2 catalog¹⁶. We correct for the difference in cosmologies assumed in our SZ analysis and that used in ACCEPT2.

6.1. Ellipsoidal Geometry

The geometry of a cluster along the line of sight can be calculated by comparing SZ and X-ray pressure profiles. If we assume azimuthal symmetry in the plane of the sky with scale radius θ_{proj} and a scale radius along the line-of-sight of θ_{los} , then we denote the elongation/compression along the line-of-sight with an axis ratio $c = \theta_{los}/\theta_{proj}$, where $c > 1$ implies that the cluster is longer along the line-of-sight than in the plane of the sky. The X-ray surface brightness is proportional to $\int n_e^2 \Lambda(T, Z) dl \propto \int (P/T)^2 \Lambda(T, Z) dl$, where Z is the abundance of heavy elements and Λ is the X-ray cooling function, while the SZ signal is proportional to $\int P dl$ (Equation 5). The temperature T can be derived from X-ray. Initially, we will assume that the cluster is spherically symmetric, and derive the pressure profile from the X-ray observations (giving P_X), and from the SZ observations (giving P_{SZ}). If the pressure profiles disagree, one explanation would be the elongation of the cluster along the line-of-sight. In this case, the elongation is given by $c = (P_{SZ}/P_X)^2$.

¹⁶ ACCEPT2 includes any publicly available *Chandra* observations, thus increasing the sample size and integration times relative to ACCEPT, as reported by Baldi (2014). A public release of ACCEPT2 is anticipated in the near future.

To estimate the ellipticity of clusters, we fit the ACCEPT2 pressure profiles with a gNFW pressure profile, with α and β fixed at their A10 values: 1.05 and 5.49, respectively. The resultant gNFW profile is then integrated along the line of sight (LOS) to create a Compton y map, and then filtered as discussed in Romero et al. (2015). For the remained of this section, we take P_{SZ} as the fitted the amplitude of the ACCEPT2 model to SZ data (i.e. $P_X \equiv 1$). Similarly, we will define P_B as the fitted the amplitude of the ACCEPT2 model to just Bolocam data.

The axis ratio is calculated as $c = P_{SZ}^2$, and its associated uncertainty is calculated as $\sigma_c^2 = 4P_{SZ}^4((\sigma_{SZ}/P_{SZ})^2 + (\sigma_X/P_X)^2)$, where $(\sigma_{SZ}/P_{SZ}) = 0.11$ and $(\sigma_X/P_X) = 0.10$ are the calibration uncertainties of Bolocam and ACCEPT2 respectively. Table 6 presents relevant fitted gNFW parameters used in calculating the cluster geometry.

The CLASH sample contains X-ray (20) and lensing (5) selected clusters and was not explicitly designed to be orientation unbiased. It is, therefore, not too surprising that we find indications that many of the clusters in our sample are elongated along the line of sight ($c > 1$). Abell 1835 is not in the CLASH sample, but is a notably well studied cool core cluster, i.e. it is the subject of many studies on the basis of its cool core.

This investigation has made the assumption that the geometry of a given cluster is globally consistent. That is, one ellipsoidal geometry applies to all regions of the cluster. However, a cluster should appear more spherical towards the center, where baryons have condensed (e.g. Kravtsov & Borgani 2012, and references therein). Also, the DM and baryonic distributions need not align (one need only look at the Bullet cluster (Markevitch et al. 2004) for a dramatic example). This is not a particular concern to this analysis as we are comparing quantities based on the baryonic distribution, but would be more of a concern when including lensing.

Across our sample, we find an average pressure ratio $\langle P_{SZ} \rangle = 1.14 \pm 0.25$, where a portion (0.07) of the uncertainty is from the scatter in the values and the dominant source of uncertainty is the statistical uncertainties of individual clusters. In elongation, we find $\langle c \rangle = 1.38 \pm 0.58$, where again, 0.33 is from the scatter. Using cosmological smooth particle hydrodynamics (SPH) simulations, Battaglia et al. (2012) find minor-to-major axis ratios $\simeq 0.85-0.9$ based on pressure distributions at $\sim R_{500}$. This ratio has some dependence on cluster mass and redshift, where in both cases the deviations from unity grow with increasing mass and with increasing redshift. As we have a heterogenous sample, there is no easy comparison with the expected scatter. As a starting point, we take the uncertainty for the $z = 0.5$ bin to be ~ 0.05 . This would then support potential values $0.8 < c < 1/0.8$, which produces tension for our results.

Working with a smaller sample than that in Battaglia et al. (2012) size (16 clusters) and higher resolution, Lau et al. (2011) use a cosmological simulation with adaptive mesh refinement (AMR) code to investigate the shape of gas and dark matter, assuming different baryonic physics in two separate runs: a radiative (CSF) and non radiative (NR) run. In relaxed clusters at R_{500} and $z = 0.6$, they find minor-to-major axis ratios

Table 6
ACCEPT2 gNFW Fitted Parameters and Comparison to SZ data

Cluster	P_0	C_{500}	γ	P_{SZ}	k	P_B	c	σ_c	$\Delta P_{SZ,B}/\sigma_{P_{SZ}}$
Abell 1835	8.1	1.4	0.44	0.83 ± 0.03	1.15	0.82 ± 0.03	0.69	0.16	0.48
Abell 611	15.3	0.9	0.62	1.31 ± 0.09	0.92	1.35 ± 0.10	1.71	0.45	0.44
MACS 1115	8.2	1.5	0.35	0.84 ± 0.05	1.14	0.80 ± 0.05	0.70	0.17	0.71
MACS 0429	6.0	1.0	0.71	1.30 ± 0.11	0.64	1.48 ± 0.11	1.70	0.47	1.56
MACS 1206	8.3	1.0	0.49	1.12 ± 0.04	1.01	1.11 ± 0.04	1.24	0.29	-0.03
MACS 0329	18.6	1.2	0.59	1.61 ± 0.09	0.90	1.64 ± 0.09	2.58	0.64	0.41
RXJ 1347	18.3	2.4	0.40	0.95 ± 0.02	1.18	0.94 ± 0.02	0.89	0.20	0.37
MACS 1311	5.8	1.6	0.26	1.28 ± 0.12	0.85	1.40 ± 0.12	1.64	0.47	0.96
MACS1423	12.1	1.8	0.51	1.26 ± 0.11	0.81	1.39 ± 0.12	1.58	0.44	1.12
MACS 1149	3.6	0.9	0.23	1.24 ± 0.06	0.70	1.28 ± 0.06	1.54	0.37	0.77
MACS 0717	21.8	1.5	0.00	1.36 ± 0.04	0.71	1.39 ± 0.04	1.85	0.43	0.54
MACS 0647	6.2	0.9	0.54	1.29 ± 0.05	1.09	1.27 ± 0.05	1.67	0.40	-0.38
MACS 0744	5.9	0.6	0.93	1.04 ± 0.06	0.94	1.05 ± 0.06	1.08	0.27	0.24
CLJ 1226	6.0	1.3	0.04	0.64 ± 0.04	1.15	0.60 ± 0.04	0.41	0.11	0.97

Note. — P_0 , C_{500} , and γ as determined by fitting the ACCEPT2 pressure profiles. P_{SZ} denotes the fitted amplitude (renormalization) of the ACCEPT2 model to the SZ data. P_B denotes the fitted amplitude of the ACCEPT2 model to just Bolocam data. We fix the gNFW parameters $\alpha = 1.05$ and $\beta = 5.49$. The elongation c is the ratio between the scale radius along the line-of-sight and the projected scale radius (taken to be azimuthally symmetric in the plane of the sky). Positive values in the column $\Delta P_{SZ,B}/\sigma_{P_{SZ}}$ indicate that the core is more spherical than the extended cluster.

of the gas distribution of 0.80 ± 0.04 and 0.72 ± 0.05 in their CSF and NR runs, respectively. For all clusters at $z = 0.6$, these values are 0.69 ± 0.05 and 0.66 ± 0.04 and correspond to elongations of 1.45 and 1.5, respectively.

Observationally, using SZ and X-ray data on a sample of 25 clusters, De Filippis et al. (2005) find a median projected elongation of 1.24 ± 0.09 , and median elongation along the line of sight (c) of 1.08 ± 0.17 , where two clusters have $c > 2.0$, and three clusters have $1.5 < c < 2.0$. Accounting for our uncertainties, only MACS 0329 and CLJ 1226 are outside (by 1σ) of the range of elongations found in the literature. While this is true, our investigations here are only concerned with elongations along the line of sight, for which we are dominated by clusters with $c > 1$. This could be due to a systematic bias of P_{SZ} high, or P_X low, or even a selection bias within the CLASH sample.

We take the difference, $\Delta P_{SZ,B} = (P_{SZ} - P_B)$ to be indicative that the gas in the core has a different elongation than ICM at moderate to large radii. In particular, for $P_B < 1$, then $P_{SZ} > P_B$ is indicative of a more spherical core and for $P_B > 1$, then a more spherical core will have $P_{SZ} < P_B$. As P_{SZ} and P_B are not independent, we approximate the uncertainty in $\Delta P_{SZ,B}$ as $\sigma_{P_{SZ}}$ and report the pseudo-significances ($\Delta P_{SZ,B}/\sigma_{P_{SZ}}$) of core sphericity (relative to the region outside the center) in Table 5. While none of our determinations individually are above 3σ , it is nonetheless interesting to note the tendency for core sphericity.

6.2. Temperature profiles

If we assume a given geometry (known ellipticity), then instead of solving for the ellipticity, we can derive a temperature profile, making use of the direct pressure constraints from SZ observations and the electron density constraints from X-ray observations. That is, we calculate

$$T_{SZ} = \frac{P_{SZ}}{n_{e,X}}, \quad (9)$$

where P_{SZ} is the pressure derived from pressure profile fits to the SZ data (Section 4) and $n_{e,X}$ is the deprojected electron density derived from X-ray data by the ACCEPT2 collaboration. For each bin, we assign radial values as the arithmetic mean of its radial bounds. Binned values of P_{SZ} are then calculated from the fitted gNFW profile for each radial value for the corresponding bins used for $n_{e,X}$.

We consider two models from the literature to describe the temperature profile: that in Vikhlinin (2006), denoted as V06, and that in Bulbul et al. (2010), denoted as B10. The first is given as:

$$T_{e,V06} = t_{cool} \times \frac{T_0}{(r/r_t)^a [1 + (r/r_t)^b]^{c/b}}, \text{ where} \quad (10)$$

$$t_{cool} = \frac{[(r/r_{cool})^{a_{cool}} + T_{min}/T_0]}{(r/r_{cool})^{a_{cool}} + 1}. \quad (11)$$

Here r_{cool} is a fitted parameter, indicated the radial scale of the cool core, r_t is a transitional radius, which has been called a scaling radius in other profiles (e.g. NFW). T_{min} is the minimum temperature observed within the cool core. We fit for the remaining parameters, a_{cool} , a , b , c , and T_0 . The first term in the V06 model (Equation 10) is denoted as the cool core taper. The second term in the V06 model (Equation 10) has the form of a gNFW profile, where typically Greek letters are used for the gNFW pressure profiles (Section 3.2). The letter equivalents are $a = \gamma$, $b = \alpha$, and $c = \beta - \gamma$. Given that for our pressure profile analysis, we fix α and β from A10 values, here we fix b and c in fitting for the V06 temperature model. We calculate c and $r_t = R_{500}/C_{500}$ based on the best fit γ and C_{500} values from our joint fits (Section 3.2). Thus, in the temperature profile, we fit for T_0 , r_{cool} , and a_{cool} , and a .

The other temperature model (Bulbul et al. 2010) is given as:

$$T_{e,B10} = T_0 \left[\frac{1}{(\beta - 2)} \frac{(1 + r/r_s)^{\beta-2} - 1}{r/r_s(1 + r/r_s)^{\beta-2}} \right] t_{cool} \quad (12)$$

where T_0 and parameters in t_{cool} are the only parameters specific to the temperature profile (independent of pressure or density profile). β is a power law term in a generalized NFW profile proposed in Bulbul et al. (2010):

$$\rho_{tot}(r) = \frac{\rho_i}{(r/r_s)(1+r/r_s)^\beta} \quad (13)$$

This formulation of density allows for an analytical formulation of $P(r)$ under the assumption of hydrostatic equilibrium. With the assumption of a polytropic equation of state ($P = k\rho_g^{n+1}$, where k is simply a constant, and n is the polytropic index), the temperature profile (Equation 12) can be derived. It is worth noting that Equation 12 does not diverge at $\beta = 2$. As with r_t in the V06 model, we fix $r_s = R_{500}/C_{500}$ based on our fitted value of C_{500} (Section 4).

We use MPFIT (Markwardt 2009) to solve for the free parameters in the two temperature profile parameterizations. For the V06 model, we fit for r_{cool} , a_{cool} , T_0 , and a , while for the B10 model we fit for r_{cool} , a_{cool} , T_0 , and β . We define our bins (annuli) based on those provided by ACCEPT2. To match to SZ instrument resolutions, we require bins be at least 5'' in width within the central arcminute, and beyond the central arcminute we require the bins be at least 30''. To meet this requirement we take the weighted average of an integer number of bins.

Our SZ and X-ray derived temperature profiles (Figure 7) reveal, on average, larger temperatures than the spectroscopically derived temperatures from ACCEPT2. Generally, both the V06 and B10 models are easily fit to our data (Table 7), as both often have $\chi^2 < 1$. Our fits do account for covariance. We note that the V06 model typically performs worse than B10 in our fits (by the goodness of fit parameter, χ^2 .) This may be due to fixing b and c (especially c) as these are fixed power laws that incorporate the behavior of n_e with radius. However, we are still fitting the same number of parameters in the two models, thus the B10 model offers more flexibility for the same number of fitted parameters.

As an additional means of comparison, we fit a profile derived in V06 for the gas mass weighted temperature:

$$\frac{T(r)}{T_{mg}} = 1.35 \frac{(x_r/0.045)^{1.9} + 0.45}{(x_r/0.045)^{1.9} + 1} \frac{1}{(1 + (x_r/0.6)^2)^{0.45}}, \quad (14)$$

where $x_r = r/R_{500}$. Thus, since we take R_{500} as known, the shape of the profile is fixed. The values fit to the ACCEPT2 temperatures are reported in Table 1. We fit T_{mg} to our T_{SZ} profiles, and compute the ratio $T_{mg,SZ}/T_{mg,X}$ of the two fitted gas mass weighted temperatures. We find that $\langle T_{mg,SZ}/T_{mg,X} \rangle = 1.38$ with a RMS scatter of 0.31.

Given the typically long exposure times (our sample has total *Chandra* exposure times, $19.5 < t_{exp} < 134.1$ ks) required to derive spectroscopic X-ray temperatures, it is likely that deriving temperatures from SZ pressure profiles and X-ray electron densities will be more commonplace as SZ instruments have progressed rapidly in recent years. We consider the how the uncertainties of two temperature derivations ($\sigma_{T_{SZ}}$ and σ_{T_X}) compare within our sample. We find that $\sigma_{T_{SZ}}$ is generally about twice as large as σ_{T_X} . Furthermore, $\sigma_{T_{SZ}}$ is dominated by both the statistical and systematic uncertainties as-

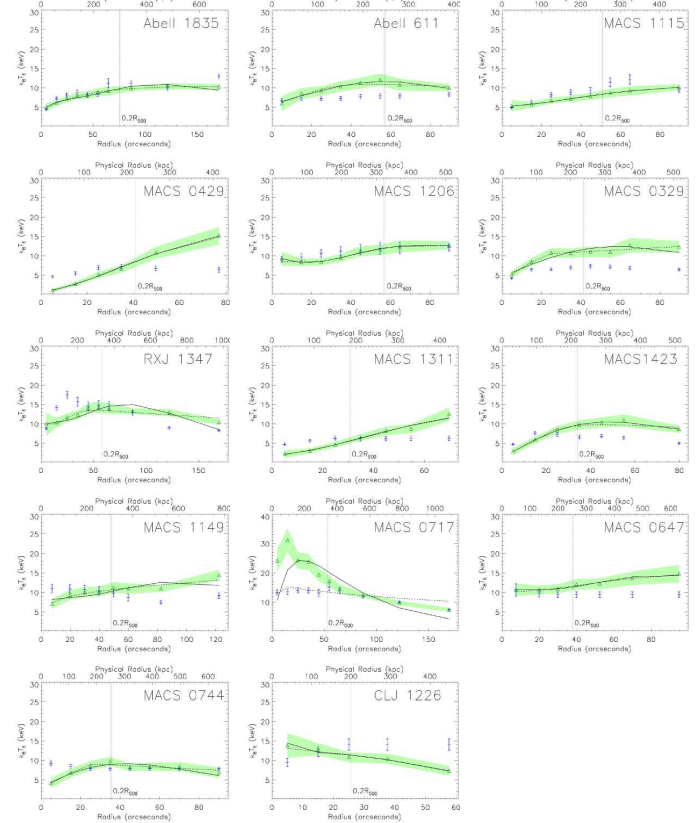


Figure 7. Temperature Profiles. The green triangles are derived as $T_{SZ} = P_{SZ}/n_{e,X}$, and the shaded green indicates 1σ uncertainties, including calibration uncertainties. The blue points are X-ray spectroscopically derived temperatures from ACCEPT2 and associated error bars. The solid lines are our fitted Vikhlinin temperature models and the dashed lines are our fitted Bulbul temperature models.

Table 7
Fitted Temperature Profiles

Cluster	χ^2_{V06}	χ^2_{B10}	DOF	$T_{mg,SZ}/T_{mg,X}$
Abell 1835	3.02	0.20	5	1.22
Abell 611	0.52	1.09	3	1.62
MACS 1115	0.17	0.14	3	1.29
MACS 0429	0.42	0.74	1	0.90
MACS 1206	0.21	0.28	3	1.27
MACS 0329	4.11	0.44	3	2.05
RXJ 1347	16.6	4.71	5	1.21
MACS 1311	1.00	0.98	2	1.48
MACS 1423	0.12	0.97	2	1.57
MACS 1149	9.25	2.32	3	1.55
MACS 0717	53.0	82.6	5	1.08
MACS 0647	0.33	0.18	2	1.69
MACS 0744	2.20	1.00	3	1.27
CLJ 1226	0.38	0.53	0	0.96

Note. — The reported χ^2 values show that the temperature error bars are generally quite large. Covariance is not taken into account. The ratio between the fitted gas mass temperatures, $T_{mg,SZ}/T_{mg,X}$, is also presented for a global comparison of temperature profiles.

sociated with P_{SZ} , where the fractional uncertainties in our SZ pressure profiles are roughly a factor of 3 larger than the fractional uncertainties in the X-ray electron densities.

Thus far, we have not taken into consideration systematic errors within σ_{T_X} . The systematic errors on T_x are not well quantified, despite evidence that these systematic errors can be notable (e.g. [Donahue et al. 2014](#)). We are thus interested in finding for what fractional systematic error do the uncertainties in σ_{TSZ} and σ_{T_X} become comparable and find that a systematic uncertainty of 20% on spectroscopic X-ray temperatures results in $\sigma_{TSZ} \sim \sigma_{T_X}$ over our sample.

We should additionally revisit our uncertainties on TSZ to consider the impact of the uncertainty of the cluster geometry on σ_{TSZ} . With consideration for elongation along the line-of-sight, $TSZ = (P_{SZ}/n_{e,X})c^{1/2}$, which will result in an additional fractional error term: $(\sigma_c/2c)$ to be added in quadrature. From [Battaglia et al. \(2012\)](#); [Lau et al. \(2011\)](#), we can likely expect this term to be of order 0.1, which is the same as the statistical and systematic uncertainties on P_{SZ} .

6.3. Discussion: Comparison Between SZ- and X-ray-Derived Quantities

We find overall agreement in ensemble constraints of the pressure profile between our SZ pressure profiles and those fitted to ACCEPT2 B14 pressure profiles (Figure 4). When calculating elongation along the line-of-sight, we find an average axis ratio $\langle c \rangle = 1.38 \pm 0.58$. In our temperature analysis, we find the average gas mass weighted temperature ratio $\langle T_{mg,SZ}/T_{mg,X} \rangle = 1.37 \pm 0.31$.

While these average values show consistency between the SZ and X-ray quantities, the SZ pressure is, on average, generally larger than the X-ray pressure, especially at larger radii. In our elongation analysis, this pressure difference is manifest as the majority of our clusters showing elongation along the line of sight, which we find is largely consistent with numerical simulations (Section 6.1). Alternatively, in our temperature analysis, we find that TSZ is generally larger than T_X , especially at larger radii. Differences in temperatures could indicate a bias of spectroscopic X-ray temperatures to lower temperatures, as emission will be dominated by the cooler (denser) regions. Moreover, *Chandra* is not sensitive to higher energy photons and therefore constraints on gas hotter than $k_B T \gtrsim 10$ keV are generally poor.

In two clusters, MACS 0717 and CLJ 1226, we attribute the differences in SZ and X-ray pressure profiles to be primarily driven by differences in temperature. The triple merging cluster MACS 0717 (Section A.11) does not present a clear shock in SZ or X-ray within the central region, but it may be that the merger activity is primarily along the line of sight. The notable enhancement of SZ-to-X-ray spectroscopic temperature in the center is undoubtedly due to merger activity, and bears credence as other studies have found hot (roughly 20 keV in [Sayers et al. \(2013\)](#); [Adam et al. \(2016\)](#), and 34 keV in [Mroczkowski et al. \(2012\)](#)) gas in the region about subcluster C, which would contribute to temperature enhancements at small radii. In CLJ 1226, the average temperature values we derive are not significantly differ-

ent than those in ACCEPT2, but the slope is reversed. In particular, the ACCEPT2 temperature in CLJ 1226 rises from 10 keV in the core to 15 keV at $r \sim 200$ kpc. In contrast, TSZ shows a more characteristic, declining temperature profile. It is unclear what would cause this difference. We believe that this difference in slope accounts for a non-trivial change in the fitted pressure profile to ACCEPT2 (Section 6.1), which drives the corresponding SZ-fitted normalizations (P_{SZ} and P_B) low.

A third cluster with notable differences in the pressure profiles is MACS 0429. The SZ and X-ray pressure profiles have considerably different shapes. While this may be due, in part, to an increase in temperature with radius, we do not contend that this increase is as dramatic as that shown in Figure 7. It is possible that the intrinsic weakness of the decrement of this cluster, combined with the unusual strength of the central source ($S_{90} = 8$ mJy), has exceeded the capabilities of our point source treatment (Section 4.1) and could thus be biasing the results on this particular cluster. However, this should primarily affect the inner pressure profile, and Bolocam is constraining the pressure at moderate to large radii to be well above that found in ACCEPT2.

Clumping may also be responsible for raising TSZ relative to T_X at larger radii. Clumping is expected to increase with radius, and thus may account for some of the discrepancy between our inferred temperature and the X-ray spectroscopically derived temperatures. [Battaglia et al. \(2015\)](#) find that clumping is more pronounced for more massive clusters. For the most massive bin of clusters considered, which is most applicable to our sample, the density clumping ($C_{2,\rho} = \langle \rho^2 \rangle / \langle \rho \rangle^2$) at R_{500} is roughly 1.2. Some SZ/X-ray constraints (e.g. [Morandi et al. 2013](#); [Morandi & Cui 2014](#)) find clumping factors $C_{2,\rho} \sim 2$ at $R_{200} \sim 1.6R_{500}$, are within agreement with simulations. A clumping factor of 1.2 can account for biasing the T_X low relative to TSZ by roughly $\sim 5\%$.

7. CONCLUSIONS

We developed an algorithm to jointly fit gNFW pressure profiles to clusters observed via the SZ effect with MUSTANG and Bolocam. We applied this algorithm to 14 clusters and found the profiles are consistent with a universal pressure profile found in [Arnaud et al. \(2010\)](#). Specifically, the pressure profile is of the form:

$$\tilde{P} = \frac{P_0}{(C_{500}X)^\gamma [1 + (C_{500}X)^\alpha]^{(\beta-\gamma)/\alpha}},$$

where we fixed α and β to values found in [Arnaud et al. \(2010\)](#). A comparison to previous determinations of pressure profiles is shown in Figure 4. Within the radii where we have the greatest constraints ($0.03R_{500} \lesssim r \lesssim R_{500}$), the pressure profile from this work is comparable to the other pressure profiles. This is further evidenced in the parameters themselves, as seen in Table 5, especially in comparison to A10 parameter values.

With the high resolution of MUSTANG, we were able to identify and remove point sources. MUSTANG is also sensitive to substructure, which we modeled and incorporated in our fitting algorithm. In the MUSTANG maps, we found that substructure in the central regions of clusters is not a rare occurrence, as four of our 14 clusters

have clearly identified substructure, and two more have potential substructure.

We find general agreement between the SZ and X-ray pressure profiles for the ensemble of our sample. Additionally, we investigated cluster geometry by taking the ratio between spherically derived pressure profiles as fit to SZ and X-ray data and we found that the clusters have an average axis ratio $\langle c \rangle = 1.38 \pm 0.58$ (individual axis ratios are tabulated in Table 6). This suggests that most of these clusters in our sample are elongated along the line of sight. This may not be surprising for a heterogeneously selected sample such as CLASH, for which several clusters were chosen for their strong lensing magnifications. We extended our analysis to estimate the relative cluster geometry in the core (from MUSTANG), compared to the larger scale ICM (from Bolocam) and we found some hint that the cores tend to be more spherical than the ICM at larger radii.

When we assumed spherical symmetry and independently calculated temperature, T_{SZ} , from SZ pressure and electron density, we found an average gas mass weighted temperature ratio $\langle T_{mg,SZ}/T_{mg,X} \rangle = 1.37 \pm 0.31$. Furthermore, our profiles of T_{SZ} reveal a trend towards higher temperatures than T_X at larger radii. We argue that higher T_{SZ} temperatures should be expected in clusters where merging activity will heat the gas beyond the sensitivity range of X-ray instruments (for *Chandra*, this is roughly $k_B T \gtrsim 10$ keV).

Cluster geometry appears to play a significant role in yielding different SZ- and X-ray-derived pressure profiles within our sample; however, it is implausible that it is the sole factor to finding larger SZ pressures than X-ray pressures. Other relevant factors such as deviations from ellipsoidal geometry; different sensitivities to hot gas in SZ and X-ray observations; and, at large radii, clumping of the ICM.

Finally, as we look forward to the future of galaxy cluster surveys (e.g. SPT3G, ACTpol, WFIRST, SPHEREx, Euclid, LSST, and eRosita), we expect ICM temperature derivations from SZ intensity and X-ray surface brightness (density) to be more common. In our study, the temperatures that we derived in this manner, T_{SZ} , are dominated by uncertainties in the SZ measurements. The fractional uncertainties in our SZ pressure profiles are roughly a factor of 3 larger than the fractional uncertainties in the X-ray electron densities. Despite this,

we find T_{SZ} uncertainties ~ 2 times larger than the statistical spectroscopic X-ray temperature uncertainties. In light of new SZ instruments (e.g. MUSTANG-2, NIKA2, and ALMA [Dicker et al. 2014](#); [Calvo et al. 2016](#); [Kitayama et al. 2016](#)) coming online with vastly improved mapping speeds, our results are encouraging for the prospects of physically characterizing the ICM of newly discovered systems with rapid follow-up programs.

ACKNOWLEDGEMENTS

While at NRAO and UVA, support for CR was provided through the Grote Reber Fellowship at NRAO. Support for CR, PK, and AY was provided by the Student Observing Support (SOS) program. Support for TM was partially provided by the National Research Council Research Associateship Award at the U.S. Naval Research Laboratory. Basic research in radio astronomy at NRL is supported by 6.1 Base funding. JS was partially supported by a Norris Foundation CCAT Postdoctoral Fellowship and by NSF/AST-1313447.

The National Radio Astronomy Observatory is a facility of the National Science Foundation which is operated under cooperative agreement with Associated Universities, Inc. The GBT observations used in this paper were taken under NRAO proposal IDs GBT/08A-056, GBT/09A-052, GBT/09C-020, GBT/09C-035, GBT/09C-059, GBT/10A-056, GBT/10C-017, GBT/10C-026, GBT/10C-031, GBT/10C-042, GBT/11A-001, and GBT/11B-009 and VLA/12A-340. We thank the GBT operators Dave Curry, Greg Monk, Dave Rose, Barry Sharp, and Donna Stricklin for their assistance.

The Bolocam observations presented here were obtained from the Caltech Submillimeter Observatory, which, when the data used in this analysis were taken, was operated by the California Institute of Technology under cooperative agreement with the National Science Foundation. Bolocam was constructed and commissioned using funds from NSF/AST-9618798, NSF/AST-0098737, NSF/AST-9980846, NSF/AST-0229008, and NSF/AST-0206158. Bolocam observations were partially supported by the Gordon and Betty Moore Foundation, the Jet Propulsion Laboratory Research and Technology Development Program, as well as the National Science Council of Taiwan grant NSC100-2112-M-001-008-MY3.

Access to ACCEPT2 data was possible due to the gracious assistance of Rachael Salmon.

APPENDIX

A. NOTES ON INDIVIDUAL CLUSTERS

A.1. *Abell 1835* ($z=0.25$)

Abell 1835 is a well studied massive cool core cluster. The cool core was noted to have substructure in the central 10'' by [Schmidt et al. \(2001\)](#), and identified as being due to the central AGN by [McNamara et al. \(2006\)](#). Abell 1835 has also been extensively studied via the SZ effect ([Reese et al. 2002](#); [Benson et al. 2004](#); [Bonamente et al. 2006](#); [Sayers et al. 2011](#); [Mauskopf et al. 2012](#)). The models adopted were either beta models or generalized beta models, and tend to suggest a shallow slope for the pressure interior to 10''. Previous analysis of Abell 1835 with MUSTANG data ([Korngut et al. 2011](#)) detected the SZ effect decrement, but not at high significance, which is consistent with a featureless, smooth, broad signal. Our updated MUSTANG reduction of Abell 1835, shown in Figure 1, has the same features as in [Korngut et al. \(2011\)](#).

A.2. Abell 611 ($z=0.29$)

The MUSTANG map (Figure 1) shows an enhancement south of the X-ray centroid, and the Bolocam map shows elongation towards the south-southwest. Weak lensing maps are suggestive of a southwest-northeast elongation (Newman et al. 2009; Zitrin et al. 2015). Using the density of galaxies, Lemze et al. (2013) find a core and a halo which align with the elongation seen in the SZ. We note that AMI (AMI Consortium et al. 2012) and De Filippis et al. (2005) also see such an elongation. De Filippis et al. (2005) also calculate a line of sight elongation $c = 1.05 \pm 0.37$. cluster in their sample and that the X-ray data presented from LaRoque et al. (2006) is very circular and uniform. Despite being relaxed, Abell 611 is not listed as a cool core cluster (nor disturbed) (Sayers et al. 2013).

In an analysis of the dark matter distribution, Newman et al. (2009) find that the core (logarithmic) slope of the cluster is shallower than an NFW model, with $\beta_{DM} = 0.3$, where the dark matter distribution has been characterized by yet another generalization of the NFW profile:

$$\rho(r) = \frac{\rho_0}{(r/r_s)^{\beta_{tot}}(1+r/r_s)^{3-\beta_{tot}}} \quad (\text{A1})$$

They find the distribution of dark matter within Abell 611 to be inconsistent with a single NFW model.

A.3. MACS 1115 ($z=0.36$)

MACS 1115 is listed as a cool core cluster (Sayers et al. 2013). It is among seven CLASH clusters that show unambiguous ultraviolet (UV) excesses attributed to unabsorbed star formation rates of 5-80 $M_{\odot}\text{yr}^{-1}$ (Donahue et al. 2015). MUSTANG detects a point source in MACS 1115, which is coincident with its BCG. MACS 1115 is fit by a fairly steep inner pressure profile slope to the SZ data (Table 5). Adopting the Bolocam centroid, the inner pressure profile slope is notably reduced, yet the goodness of fit is not significantly changed. In particular, the Bolocam image shows a north-south elongation (particularly to the north of the centroids). In contrast, weak and strong lensing (Zitrin et al. 2015) show a more southeast-northwest elongation.

A.4. MACS 0429 ($z=0.40$)

MACS 0429 has been well studied in the X-ray (Schmidt & Allen 2007; Comerford & Natarajan 2007; Maughan et al. 2008; Allen et al. 2008; Mann & Ebeling 2012) MACS 0429 is identified as a cool core cluster (cf. Mann & Ebeling 2012; Sayers et al. 2013). The bright point source in the MUSTANG image is the cluster BCG, which is noted as having an excesses UV emission (Donahue et al. 2015). Of the point sources observed by MUSTANG, this has the shallowest spectral index between 90 GHz and 140 GHz of $\alpha_{\nu} = 0.55$.

Despite MACS 0429's stature as a cool core cluster, its pressure profile (Table 5) is surprisingly shallow in the core, and shows elevated pressure relative to X-ray derived pressure at moderate radii. The offset between the Bolocam centroid (Sayers et al. 2013) and ACCEPT (Cavagnolo et al. 2009) centroid is 100 kpc, which is notably larger than the X-ray-optical separations of the cluster peaks and centroids reported in Mann & Ebeling (2012) of 12.8 and 19.5 kpc respectively. Siegel et al. (in prep.) report an excess in SZ pressure (Bolocam) relative to X-ray (*Chandra*) pressure at moderate to large radii.

A.5. MACS 1206 ($z=0.44$)

MACS 1206 has been observed extensively (e.g. Ebeling et al. 2001, 2009; Gilmour et al. 2009; Umetsu et al. 2012; Zitrin et al. 2012b; Biviano et al. 2013; Sayers et al. 2013). It is not categorized as a cool core or a disturbed cluster (Sayers et al. 2013). Using weak lensing data from Subaru, Umetsu et al. (2012) find that the major-minor axis ratio of projected mass is $\gtrsim 1.7$ at 1σ . They infer that this high ellipticity and alignment with the BCG, optical, X-ray, and LSS shapes are suggestive that the major axis is aligned close to the plane of the sky. In Young et al. (2015), substructure is identified that corresponds to an optically-identified subcluster, which may either be a merging subcluster, or a foreground cluster. In this analysis, the SZ signal observed by MUSTANG is well modelled by a residual component (coincident with the subcluster) and a spherical bulk ICM component. We note that the Bolocam contours of MACS 1206 do not exhibit much ellipticity. We do find that MACS 1206 has a major-minor axis ratio of 1.24 ± 0.29 (Table 6), where the major axis is along the line of sight.

A.6. MACS 0329 ($z=0.45$)

MACS 0329 has the distinction of being listed as both a cool core and disturbed cluster. Although it has been classified as relaxed (Schmidt & Allen 2007), substructure has been noted (Maughan et al. 2008), and it earns its cool core and disturbed classifications based on central weighting of X-ray luminosity and comparing centroid offsets between optical and X-ray data (Sayers et al. 2013). The elongation of the weak lensing and strong lensing are towards the northwest and southeast of the centroid.

MACS 0329 has two systems with multiple images: one at $z = 6.18$ and the other at $z = 2.17$. The Einstein radii for these two systems are $r_E = 34''$ and $r_E = 28''$, respectively (Zitrin et al. 2012a), which is noted as being typical for relaxed, well-concentrated lensing clusters.

A.7. RXJ1347 ($z=0.45$)

RXJ1347 is one of the most luminous X-ray clusters, and has been well studied in radio, SZ, lensing, optical spectroscopy, and X-rays (e.g. Schindler et al. 1995; Allen et al. 2002; Pointecouteau et al. 1999; Komatsu et al. 2001;

Kitayama et al. 2004; Gitti et al. 2007a; Ota et al. 2008; Bradač et al. 2008; Miranda et al. 2008). X-ray contours have long suggested RXJ1347 is a relaxed system (e.g. Schindler et al. 1997), and it is classified as a cool core cluster (e.g. Mann & Ebeling 2012; Sayers et al. 2013).

Indeed, the first sub-arcminute SZ observations (Komatsu et al. 2001; Kitayama et al. 2004) saw an enhancement to the southeast of the cluster X-ray peak, which was suggested as being due to shock heating. This enhancement was confirmed by MUSTANG (Mason et al. 2010). Further measurements were made with CARMA (Plagge et al. 2013), which find the 9% of the thermal energy in the cluster is in sub-arcminute substructure. Most recently, Kitayama et al. (2016) has observed this cluster with ALMA to a resolution of 5''. At low radio frequencies (Ferrari et al. 2011, 237 MHz and 614 MHz), (Gitti et al. 2007b, 1.4 GHz) find evidence for a radio mini-halo in the core of RXJ1347. The cosmic ray electrons are thought to be reaccelerated because of the shock and sloshing in the cluster (Ferrari et al. 2011).

We observe a point source (coincident with the BCG) with flux density of 7.40 ± 0.58 mJy. Previous analysis of the MUSTANG data found the point source flux density as 5 mJy (Mason et al. 2010). The difference in the flux densities is likely accounted by (1) the different modeling of point sources; primarily that we filter the double Gaussian, (2) we simultaneously fit the components, and (3) we assume a steeper profile in the core than the beta model assumed in Mason et al. (2010). Lower frequency radio observations found the flux density of the source to be 10.81 ± 0.19 mJy at 28.5 GHz (Reese et al. 2002), and 47.6 ± 1.9 mJy at 1.4 GHz (Condon et al. 1998). The BCG is observed to have a UV excess (Donahue et al. 2015).

Despite the classification of being a cool core cluster, it is also observed that there are hot regions, intially constrained as $k_B T > 10$ keV (e.g. Allen et al. 2002; Bradač et al. 2008), and more recently constrained to even hotter temperatures ($k_B T > 20$ keV Johnson et al. 2012), indicative of an unrelaxed cluster. Johnson et al. (2012) also interpret the two cold fronts as being due to sloshing, where a subscluster has returned for a second passage.

Several previous studies have found similar evidence for compression along the line of sight in this cluster (e.g. Plagge et al. 2013, and references therein). However, the compression we find in this study is less severe as in Plagge et al. (2013).

A.8. MACS 1311 ($z=0.49$)

MACS 1311 is listed as a cool core cluster (e.g. Sayers et al. 2013), and appears to have quite circular contours in the X-ray and lensing images, yet has evidence for some disturbance, given its classification in Mann & Ebeling (2012). However, the SZ contours from Bolocam show some enhancement to the west, and has a notable centroid shift (27.7'', 167 kpc) westward from the X-ray centroid. When fitting pressure profiles to this cluster, it appears that the enhanced SZ pressure at moderate radii ($r \sim 100''$) is due to this enhancement, especially when noting that we use the X-ray centroid. Adopting the Bolocam centroid does not change the pressure profile much, and we still observe a pressure enhancement at moderate radii. In contrast, in their analysis, Siegel et al. (in prep.) find that X-ray (*Chandra*) and SZ (Bolocam) data are in good agreement with a spherical ICM model which is supported primarily with thermal pressure.

A.9. MACS 1423 ($z=0.54$)

MACS 1423 is a cool core cluster (Mann & Ebeling 2012; Sayers et al. 2013). While the Bolocam contours are quite concentric, and suggestive of a relaxed cluster, the centroid is still offset from the X-ray peak by an appreciable angle (19.8'', 126 kpc). Similar to MACS 1311, the pressure is slightly less than the ACCEPT2 X-ray derived pressure in the core, and slightly greater at moderate radii. While this is expected for a centroid offset, we find that adopting the Bolocam centroid again yields no substantial difference in the SZ pressure profile. Both our analysis and that of Siegel et al. (in prep.) find good agreement between SZ and X-ray pressure profiles. We observe a point source (the cluster BCG) with flux density of 1.36 ± 0.13 mJy, which is also observed to have a UV excess (Donahue et al. 2015).

A.10. MACS 1149 ($z=0.54$)

MACS 1149 is classified as a disturbed cluster (e.g. Mann & Ebeling 2012; Sayers et al. 2013), and lensing studies have found that a single DM halo does not describe the cluster well, but rather at least four large-scale DM halos are used to describe the cluster (Smith et al. 2009). A large radial velocity dispersion (1800 km s^{-1} Ebeling et al. 2007) is observed, indicative of merger activity along the line of sight. X-ray, SZ, and lensing (particularly strong lensing) all show elongation in the northwest-southeast direction. Most recently, Golovich et al. (2016) investigate the dynamics of the cluster, identifying three subclusters, with merger activity (velocities) primarily in the plane of the sky.

While the Bolocam map of this cluster shows a modest elongation in the northwest-southeast direction, it is well modelled as a spherical cluster. Our SZ derived pressure profile roughly matches the shape of the X-ray derived pressure profile, with the SZ pressure consistently greater than the X-ray pressure. We calculate that the axis along the line of sight is 1.54 ± 0.37 (Section 6.1) times greater than the axes in the plane of the sky. In the MUSTANG map, we see a 3σ feature to the east of the centroids, but it is not clear that this is associated with any particular feature.

A.11. MACS 0717 ($z=0.55$)

Despite MACS 1149's impressive merging activity, MACS 0717 is thought to be the most disturbed massive cluster at $z > 0.5$ (Ebeling et al. 2007), which appears to be accreting matter along a 6-Mpc-long filament (Ebeling et al.

2004), and has the largest known Einstein radius ($\theta_e \sim 55''$; Zitrin et al. 2009). Four distinct components are identified from X-ray and optical analyses (Ma et al. 2009), and the lensing analyses (Zitrin et al. 2009; Limousin et al. 2012) find agreement in the location of these four mass peaks with those from the X-ray and optical.

There are four identified subclusters (labeled A through D Ma et al. 2009). They find that subcluster C is the most massive component, while subcluster A is the least massive, and subclusters B and D are likely remnant cores. The velocities of the components from spectroscopy are found to be $(v_A, v_B, v_C, v_D) = (+278^{+295}_{-339}, +3238^{+252}_{-242}, -733^{+486}_{-478}, +831^{+843}_{-800}) \text{ km s}^{-1}$ (Ma et al. 2009). The first indication of detection of the kSZ signal towards these subclusters was presented in Mroczkowski et al. (2012), with a subsequent paper from Sayers et al. (2013) having the first significant detection and derived cluster velocities. Most recently, Adam et al. (2016) has mapped the kSZ signal and derived model-dependent subcluster velocities.

MACS 0717 has also been observed at 610 MHz with the Giant Metrewave Radio Telescope (GMRT) which reveals both a radio halo and a radio relic (van Weeren et al. 2009). This is interpreted as likely being due to a diffuse shock acceleration (DSA).

We observe a foreground radio galaxy, well outside the cluster centered, which we model as a point source here, with flux density of $2.08 \pm 0.25 \text{ mJy}$ at 90 GHz. This was previously reported with an integrated flux density of $2.8 \pm 0.2 \text{ mJy}$ and an extended shape $14.^{\circ}4 \times 16.^{\circ}1$ (Mroczkowski et al. 2012). However, an improved beam modeling has allowed us to model the foreground galaxy given a known beam shape. It is also worth noting that the MUSTANG data itself has been processed slightly differently from that presented in Mroczkowski et al. (2012); in this work the map is produced with a common calculated as the mean across detectors, whereas in Mroczkowski et al. (2012) the common mode was calculated as the median across detectors.

A.12. MACS 0647 ($z=0.59$)

MACS 0647 is at $z = 0.591$ and is classified as neither a cool core nor a disturbed cluster (Sayers et al. 2013). It was included in the CLASH sample due to its strong lensing properties (Postman et al. 2012). Gravitational lensing (Zitrin et al. 2011), X-ray surface brightness (Mann & Ebeling 2012), and SZ effect (MUSTANG, see Figure 1, and Bolocam) maps all show elongation in an east-west direction. In the joint analysis presented here, we see that the spherical model provides an adequate fit to both datasets and we note that the spherical assumption allows for a easier interpretation of the mass profile of the cluster.

A.13. MACS 0744 ($z=0.70$)

MACS 0744 is neither classified as a cool core cluster nor a disturbed cluster (Mann & Ebeling 2012; Sayers et al. 2013), but qualifies as a relaxed cluster (Mann & Ebeling 2012). There is a dense X-ray core, and a doubly peaked red sequence of galaxies as found by Kartaltepe et al. (2008). The gas is also found to be rather hot: $k_B T = 17.9^{+10.8}_{-3.4} \text{ keV}$, as determined by combining SZ and X-ray data (LaRoque et al. 2003).

The data presented here is the same as in Korngut et al. (2011), but has been processed differently: again, the primary difference is in the treatment of the common mode. Additionally, Korngut et al. (2011) optimize over the low-pass filtering of the common mode and do not implement a correction factor for the SNR map. The surface brightness significance of the shock feature is the same, but is perhaps less bowed than the kidney bean shape seen previously. The excess found in Korngut et al. (2011) marked the first clear detection of a shock in the SZ that had not been previously been known from X-ray observations. Korngut et al. (2011) reanalyze the X-ray data with the knowledge of the shocked region from MUSTANG, and calculate the Mach number of the shock based on (1) the shock density jump, (2) stagnation condition between the pressures at the edge of the cold front and just ahead of the shock, and (3) temperature jump across the shock, and find Mach numbers between 1.2 and 2.1, with a velocity of $1827^{+267}_{-195} \text{ km s}^{-1}$. The shocked region (region II in Korngut et al. (2011)) is well modelled with 19.7 keV gas.

A.14. CLJ 1226 ($z=0.89$)

CLJ 1226 is a well studied high redshift cluster (e.g. Mroczkowski et al. 2009; Bulbul et al. 2010; Adam et al. 2015). Adam et al. (2015) find a point source at RA 12:12:00.01 and Dec +33:32:42 with a flux density of $6.8 \pm 0.7 \text{ (stat.)} \pm 1.0 \text{ (cal.) mJy}$ at 260 GHz and $1.9 \pm 0.2 \text{ (stat.)}$ at 150 GHz. This is not the same point source seen in Korngut et al. (2011), which is reported as a point source with 4.6σ significance in surface brightness, and can be fit in our current analysis as a point source with a flux density of $0.33 \pm 0.13 \text{ mJy}$. A short VLA filler observation (VLA-12A-340, D-array, at 7 GHz) was performed to follow up this potential source. To a limit of $\sim 50\mu\text{Jy}$ nothing is seen, other than the clearly spatially distinct radio source associated with the BCG at the cluster center (1 mJy at 7 GHz and 3.2 mJy in NVSS). In contrast, the point source found in Adam et al. (2015) is fit to our data with a flux density of $0.36 \pm 0.11 \text{ mJy}$. Given the slight increase in significance of the point source from Adam et al. (2015), we adopt that point source location for our pressure profile analysis of CLJ 1226.

In the previous analysis of the MUSTANG data, Korngut et al. (2011) find a ridge of significant substructure after subtracting a bulk SZ profile (N07, fitted to SZA data). They find that this ridge, southwest of the cluster center, alongside X-ray profiles, are consistent with a merger scenario. However, in this work, we do not find any significant substructure after fitting a bulk component.

B. DATA PRODUCTS

We have made MUSTANG data products for the sample of clusters analysed in this paper available at: https://safe.nrao.edu/wiki/bin/view/GB/Pennarray/MUSTANG_CLASH. Links to accompanying Bolocam and ACCEPT data are available from this website as well. In particular, we have publicized the final data maps, noise maps, and signal-to-noise (SNR) maps used in this analysis, as well as transfer functions for individual clusters. Further documentation is available on the website.

REFERENCES

Abramopoulos, F., Chanan, G. A., & Ku, W. H.-M. 1981, *ApJ*, 248, 429

Adam, R., Comis, B., Macías-Pérez, J.-F., et al. 2015, *A&A*, 576, A12

Adam, R., Bartalucci, I., Pratt, G. W., et al. 2016, ArXiv e-prints

Allen, S. W., Rapetti, D. A., Schmidt, R. W., et al. 2008, *MNRAS*, 383, 879

Allen, S. W., Schmidt, R. W., & Fabian, A. C. 2002, *MNRAS*, 335, 256

AMI Consortium, Hurley-Walker, N., Bridle, S., et al. 2012, *MNRAS*, 419, 2921

Arnaud, M., Pratt, G. W., Piffaretti, R., et al. 2010, *A&A*, 517, A92

Baldi, A. 2014, in 15 Years of Science with Chandra, Posters from the Chandra Science Symposium held 18-21 November, 2014 in Boston, MA., id.P8, P8

Battaglia, N., Bond, J. R., Pfrommer, C., & Sievers, J. L. 2012, *ApJ*, 758, 75

—. 2015, *ApJ*, 806, 43

Benson, B. A., Church, S. E., Ade, P. A. R., et al. 2004, *ApJ*, 617, 829

Biviano, A., Rosati, P., Balestra, I., et al. 2013, *A&A*, 558, A1

Bonamente, M., Joy, M. K., LaRoque, S. J., et al. 2006, *ApJ*, 647, 25

Bonamente, M., Hasler, N., Bulbul, E., et al. 2012, *New Journal of Physics*, 14, 025010

Borgani, S., Murante, G., Springel, V., et al. 2004, *MNRAS*, 348, 1078

Bradač, M., Schrabback, T., Erben, T., et al. 2008, *ApJ*, 681, 187

Bulbul, G. E., Hasler, N., Bonamente, M., & Joy, M. 2010, *ApJ*, 720, 1038

Calvo, M., Benoit, A., Catalano, A., et al. 2016, *Journal of Low Temperature Physics*, 184, 816

Cavagnolo, K. W., Donahue, M., Voit, G. M., & Sun, M. 2008, *ApJ*, 682, 821

—. 2009, *ApJS*, 182, 12

Comerford, J. M., & Natarajan, P. 2007, *MNRAS*, 379, 190

Condon, J. J., Cotton, W. D., Greisen, E. W., et al. 1998, *AJ*, 115, 1693

Crawford, C. S., Allen, S. W., Ebeling, H., Edge, A. C., & Fabian, A. C. 1999, *MNRAS*, 306, 857

Czakon, N. G., Sayers, J., Mantz, A., et al. 2015, *ApJ*, 806, 18

De Filippis, E., Sereno, M., Bautz, M. W., & Longo, G. 2005, *ApJ*, 625, 108

Dicker, S. R., Korngut, P. M., Mason, B. S., et al. 2008, in Society of Photo-Optical Instrumentation Engineers (SPIE) Conference Series, Vol. 7020, Society of Photo-Optical Instrumentation Engineers (SPIE) Conference Series

Dicker, S. R., Ade, P. A. R., Aguirre, J., et al. 2014, in Society of Photo-Optical Instrumentation Engineers (SPIE) Conference Series, Vol. 9153, Society of Photo-Optical Instrumentation Engineers (SPIE) Conference Series, 0

Donahue, M., Voit, G. M., Mahdavi, A., et al. 2014, *ApJ*, 794, 136

Donahue, M., Connor, T., Fogarty, K., et al. 2015, ArXiv e-prints

Ebeling, H., Barrett, E., & Donovan, D. 2004, *ApJL*, 609, L49

Ebeling, H., Barrett, E., Donovan, D., et al. 2007, *ApJL*, 661, L33

Ebeling, H., Edge, A. C., & Henry, J. P. 2001, *ApJ*, 553, 668

Ebeling, H., Ma, C. J., Kneib, J.-P., et al. 2009, *MNRAS*, 395, 1213

Fabian, A. C., Sanders, J. S., Taylor, G. B., et al. 2006, *MNRAS*, 366, 417

Ferrari, C., Intema, H. T., Orrù, E., et al. 2011, *A&A*, 534, L12

Gilfanov, M. R., & Syunyaev, R. A. 1984, *Soviet Astronomy Letters*, 10, 137

Gilmour, R., Best, P., & Almaini, O. 2009, *MNRAS*, 392, 1509

Gitti, M., Ferrari, C., Domainko, W., Feretti, L., & Schindler, S. 2007a, *A&A*, 470, L25

Gitti, M., Piffaretti, R., & Schindler, S. 2007b, *A&A*, 475, 441

Glenn, J., Bock, J. J., Chattopadhyay, G., et al. 1998, *Proc. SPIE*, 3357, 326

Golovich, N., Dawson, W. A., Wittman, D., et al. 2016, ArXiv e-prints

Haig, D. J., Ade, P. A. R., Aguirre, J. E., et al. 2004, in Society of Photo-Optical Instrumentation Engineers (SPIE) Conference Series, Vol. 5498, Society of Photo-Optical Instrumentation Engineers (SPIE) Conference Series, ed. C. M. Bradford, P. A. R. Ade, J. E. Aguirre, J. J. Bock, M. Dragovan, L. Duband, L. Earle, J. Glenn, H. Matsuhara, B. J. Naylor, H. T. Nguyen, M. Yun, & J. Zmuidzinas, 78–94

Hasselfield, M., Hilton, M., Marriage, T. A., et al. 2013, *J. Cosmology Astropart. Phys.*, 7, 8

Jewell, P. R., & Prestage, R. M. 2004, in Society of Photo-Optical Instrumentation Engineers (SPIE) Conference Series, Vol. 5489, Ground-based Telescopes, ed. J. M. Oschmann, Jr., 312–323

Johnson, R. E., Zuhone, J., Jones, C., Forman, W. R., & Markevitch, M. 2012, *ApJ*, 751, 95

Kartaltepe, J. S., Ebeling, H., Ma, C. J., & Donovan, D. 2008, *MNRAS*, 389, 1240

Kitayama, T., Komatsu, E., Ota, N., et al. 2004, *PASJ*, 56, 17

Kitayama, T., Ueda, S., Takakuwa, S., et al. 2016, ArXiv e-prints

Komatsu, E., Matsuo, H., Kitayama, T., et al. 2001, *PASJ*, 53, 57

Korngut, P. M., Dicker, S. R., Reese, E. D., et al. 2011, *ApJ*, 734, 10

Kravtsov, A. V., & Borgani, S. 2012, *ARA&A*, 50, 353

LaRoque, S. J., Bonamente, M., Carlstrom, J. E., et al. 2006, *ApJ*, 652, 917

LaRoque, S. J., Joy, M., Carlstrom, J. E., et al. 2003, *ApJ*, 583, 559

Lau, E. T., Nagai, D., Kravtsov, A. V., & Zentner, A. R. 2011, *ApJ*, 734, 93

Lemze, D., Postman, M., Genel, S., et al. 2013, *ApJ*, 776, 91

Limousin, M., Ebeling, H., Richard, J., et al. 2012, *A&A*, 544, A71

Ma, C.-J., Ebeling, H., & Barrett, E. 2009, *ApJL*, 693, L56

Mann, A. W., & Ebeling, H. 2012, *MNRAS*, 420, 2120

Mantz, A., Allen, S. W., Rapetti, D., & Ebeling, H. 2010, *MNRAS*, 406, 1759

Mantz, A. B., Allen, S. W., Morris, R. G., & Schmidt, R. W. 2016, *MNRAS*, 456, 4020

Markevitch, M., Gonzalez, A. H., Clowe, D., et al. 2004, *ApJ*, 606, 819

Markevitch, M., & Vikhlinin, A. 2007, *Phys. Rep.*, 443, 1

Markwardt, C. B. 2009, in Astronomical Society of the Pacific Conference Series, Vol. 411, Astronomical Data Analysis Software and Systems XVIII, ed. D. A. Bohlender, D. Durand, & P. Dowler, 251

Mason, B. S., Dicker, S. R., Korngut, P. M., et al. 2010, *ApJ*, 716, 739

Maughan, B. J., Jones, C., Forman, W., & Van Speybroeck, L. 2008, *ApJS*, 174, 117

Mauskopf, P. D., Horner, P. F., Aguirre, J., et al. 2012, *MNRAS*, 421, 224

McDonald, M., Benson, B. A., Vikhlinin, A., et al. 2014, *ApJ*, 794, 67

McNamara, B. R., & Nulsen, P. E. J. 2007, *ARA&A*, 45, 117

McNamara, B. R., Rafferty, D. A., Bîrzan, L., et al. 2006, *ApJ*, 648, 164

McNamara, B. R., Russell, H. R., Nulsen, P. E. J., et al. 2014, *ApJ*, 785, 44

Miranda, M., Sereno, M., de Filippis, E., & Paolillo, M. 2008, *MNRAS*, 385, 511

Morandi, A., & Cui, W. 2014, *MNRAS*, 437, 1909

Morandi, A., Nagai, D., & Cui, W. 2013, *MNRAS*, 436, 1123

Morandi, A., Sun, M., Forman, W., & Jones, C. 2015, ArXiv e-prints

Mroczkowski, T., Bonamente, M., Carlstrom, J. E., et al. 2009, *ApJ*, 694, 1034

Mroczkowski, T., Dicker, S., Sayers, J., et al. 2012, *ApJ*, 761, 47

Nagai, D., Kravtsov, A. V., & Vikhlinin, A. 2007, *ApJ*, 668, 1

Nagai, D., & Lau, E. T. 2011, *ApJL*, 731, L10

Navarro, J. F., Frenk, C. S., & White, S. D. M. 1997, *ApJ*, 490, 493

Nelson, K., Lau, E. T., & Nagai, D. 2014, *ApJ*, 792, 25

Newman, A. B., Treu, T., Ellis, R. S., et al. 2009, *ApJ*, 706, 1078

O'Dea, K. P., Quillen, A. C., O'Dea, C. P., et al. 2010, *ApJ*, 719, 1619

Ota, N., Murase, K., Kitayama, T., et al. 2008, *A&A*, 491, 363

Peng, F., & Nagai, D. 2009, *ApJ*, 693, 839

Plagge, T. J., Marrone, D. P., Abdulla, Z., et al. 2013, *ApJ*, 770, 112

Planck Collaboration, Ade, P. A. R., Aghanim, N., et al. 2013, *A&A*, 558, C2

Pointecouteau, E., Giard, M., Benoit, A., et al. 1999, *ApJL*, 519, L115

Postman, M., Coe, D., Benítez, N., et al. 2012, *ApJS*, 199, 25

Pratt, G. W., Arnaud, M., Piffaretti, R., et al. 2010, *A&A*, 511, A85

Reese, E. D., Carlstrom, J. E., Joy, M., et al. 2002, *ApJ*, 581, 53

Reichardt, C. L., Stalder, B., Bleem, L. E., et al. 2013, *ApJ*, 763, 127

Romero, C., Mason, B. S., Sayers, J., et al. 2015, ArXiv e-prints

Sayers, J., Czakon, N. G., Bridge, C., et al. 2012, *ApJL*, 749, L15

Sayers, J., Golwala, S. R., Ameglio, S., & Pierpaoli, E. 2011, *ApJ*, 728, 39

Sayers, J., Czakon, N. G., Mantz, A., et al. 2013, *ApJ*, 768, 177

Schindler, S., Hattori, M., Neumann, D. M., & Boehringer, H. 1997, *A&A*, 317, 646

Schindler, S., Guzzo, L., Ebeling, H., et al. 1995, *A&A*, 299, L9

Schmidt, R. W., & Allen, S. W. 2007, *MNRAS*, 379, 209

Schmidt, R. W., Allen, S. W., & Fabian, A. C. 2001, *MNRAS*, 327, 1057

Shaw, L. D., Nagai, D., Bhattacharya, S., & Lau, E. T. 2010, *ApJ*, 725, 1452

Smith, G. P., Ebeling, H., Limousin, M., et al. 2009, *ApJL*, 707, L163

Sunyaev, R. A., & Zel'dovich, Y. B. 1972, *Comments Astrophys. Space Phys.*, 4, 173

Umetsu, K., Medezinski, E., Nonino, M., et al. 2012, *ApJ*, 755, 56

van Weeren, R. J., Röttgering, H. J. A., Brüggen, M., & Cohen, A. 2009, *A&A*, 505, 991

Vikhlinin, A. 2006, *ApJ*, 640, 710

Vikhlinin, A., Kravtsov, A., Forman, W., et al. 2006, *ApJ*, 640, 691

Young, A. H., Mroczkowski, T., Romero, C., et al. 2015, *ApJ*, 809, 185

Zitrin, A., Broadhurst, T., Barkana, R., Rephaeli, Y., & Benítez, N. 2011, *MNRAS*, 410, 1939

Zitrin, A., Broadhurst, T., Rephaeli, Y., & Sadeh, S. 2009, *ApJL*, 707, L102

Zitrin, A., Moustakas, J., Bradley, L., et al. 2012a, *ApJL*, 747, L9

Zitrin, A., Rosati, P., Nonino, M., et al. 2012b, *ApJ*, 749, 97

Zitrin, A., Fabris, A., Merten, J., et al. 2015, *ApJ*, 801, 44